



The Sloan Digital Sky Survey Quasar Catalog: Sixteenth Data Release

Brad W. Lyke¹, Alexandra N. Higley¹, J. N. McLane¹, Danielle P. Schurhammer¹, Adam D. Myers¹, Ashley J. Ross², Kyle Dawson³, Solène Chabanier⁴, Paul Martini^{2,5}, Nicolás G. Busca⁶, Hélion du Mas des Bourboux³, Mara Salvato⁷, Alina Streblyanska^{8,9}, Pauline Zarrouk^{4,10}, Etienne Burtin⁴, Scott F. Anderson¹¹, Julian Bautista¹², Dmitry Bizyaev^{13,14}, W. N. Brandt^{15,16,17}, Jonathan Brinkmann¹³, Joel R. Brownstein³, Johan Comparat⁷, Paul Green¹⁸, Axel de la Macorra¹⁹, Andrea Muñoz Gutiérrez¹⁹, Jiamin Hou⁷, Jeffrey A. Newman²⁰, Nathalie Palanque-Delabrouille⁴, Isabelle Pâris³⁰, Will J. Percival^{21,22,23}, Patrick Petitjean²⁴, James Rich⁴, Graziano Rossi²⁵, Donald P. Schneider^{16,26}, Alexander Smith⁴, M. Vivek^{27,28}, and Benjamin Alan Weaver²⁹

¹ University of Wyoming, 1000 E. University Avenue, Laramie, WY 82071, USA; blyke@uwyo.edu

² The Center of Cosmology and Astro-Particle Physics, Ohio State University, Columbus, OH, USA

³ Department of Physics and Astronomy, University of Utah, 115 S. 1400 E, Salt Lake City, UT 84112, USA

⁴ IRFU, CEA, Centre d'Etudes Saclay, F-91191 Gif-Sur-Yvette Cedex, France

⁵ Department of Astronomy, The Ohio State University, 140 W. 18th Avenue, Columbus, OH 43210, USA

⁶ Sorbonne Université, CNRS/IN2P3, Laboratoire de Physique Nucléaire et de Hautes Energies, LPNHE, 4 Place Jussieu, F-75252, Paris, France

⁷ Max-Planck-Institut für Extraterrestrische Physik, Giessenbachstraße 1, D-85748 Garching, Germany

⁸ Instituto de Astrofísica de Canarias (IAC), E-38200 La Laguna, Tenerife, Spain

⁹ Universidad de La Laguna (ULL), Dept. Astrofísica, E-38206 La Laguna, Tenerife, Spain

¹⁰ Institute for Computational Cosmology, Department of Physics, Durham University, South Road, Durham, DH1 3LE, UK

¹¹ Department of Astronomy, University of Washington, Box 351580, Seattle, WA 98195, USA

¹² Institute of Cosmology & Gravitation, University of Portsmouth, Dennis Sciama Building, Portsmouth, PO1 3FX, UK

¹³ Apache Point Observatory and New Mexico State University, P.O. Box 59, Sunspot, NM, 88349-0059, USA

¹⁴ Sternberg Astronomical Institute, Moscow State University, Moscow, Russia

¹⁵ Department of Astronomy & Astrophysics, 525 Davey Lab, The Pennsylvania State University, University Park, PA 16802, USA

¹⁶ Institute for Gravitation and the Cosmos, The Pennsylvania State University, University Park, PA 16802, USA

¹⁷ Department of Physics, 104 Davey Lab, The Pennsylvania State University, University Park, PA 16802, USA

¹⁸ Harvard-Smithsonian Center for Astrophysics, 60 Garden Street, MS #20, Cambridge, MA 02138, USA

¹⁹ Instituto de Física, Universidad Nacional Autónoma de México, Apdo. Postal 20-364, Mexico

²⁰ Pitt PACC, Department of Physics and Astronomy, University of Pittsburgh, Pittsburgh, PA 15260, USA

²¹ Waterloo Centre for Astrophysics, University of Waterloo, 200 University Avenue W, Waterloo, ON N2L 3G1, Canada

²² Department of Physics and Astronomy, University of Waterloo, 200 University Avenue W, Waterloo, ON N2L 3G1, Canada

²³ Perimeter Institute for Theoretical Physics, 31 Caroline Street North, Waterloo, ON N2L 2Y5, Canada

²⁴ Institut d'Astrophysique de Paris, Sorbonne Universités and CNRS, 98bis Boulevard Arago, F-75014 Paris, France

²⁵ Department of Astronomy and Space Science, Sejong University, 209, Neungdong-ro, Gwangjin-gu, Seoul, Republic of Korea

²⁶ Department of Astronomy and Astrophysics, The Pennsylvania State University, University Park, PA 16802, USA

²⁷ Indian Institute of Astrophysics, Koramangala, Bangalore 560034, India

²⁸ 525, Davey Lab, Pennsylvania State University, State College, PA 16802, USA

²⁹ NSF's National Optical-Infrared Astronomy Research Laboratory, 950 North Cherry Avenue, Tucson, AZ 85719, USA

Received 2020 April 28; revised 2020 July 10; accepted 2020 July 13; published 2020 August 27

Abstract

We present the final Sloan Digital Sky Survey IV (SDSS-IV) quasar catalog from Data Release 16 of the extended Baryon Oscillation Spectroscopic Survey (eBOSS). This catalog comprises the largest selection of spectroscopically confirmed quasars to date. The full catalog includes two subcatalogs (the current versions are DR16Q_v4 and DR16Q_Superset_v3 at <https://data.sdss.org/sas/dr16/eboss/qso/DR16Q/>): a “superset” of all SDSS-IV/eBOSS objects targeted as quasars containing 1,440,615 observations and a quasar-only catalog containing 750,414 quasars, including 225,082 new quasars appearing in an SDSS data release for the first time, as well as known quasars from SDSS-I/II/III. We present automated identification and redshift information for these quasars alongside data from visual inspections for 320,161 spectra. The quasar-only catalog is estimated to be 99.8% complete with 0.3%–1.3% contamination. Automated and visual inspection redshifts are supplemented by redshifts derived via principal component analysis and emission lines. We include emission-line redshifts for H α , H β , Mg II, C III], C IV, and Ly α . Identification and key characteristics generated by automated algorithms are presented for 99,856 broad absorption-line quasars and 35,686 damped Lyman alpha quasars. In addition to SDSS photometric data, we also present multiwavelength data for quasars from the Galaxy Evolution Explorer, UKIDSS, the Wide-field Infrared Survey Explorer, FIRST, ROSAT/2RXS, XMM-Newton, and Gaia. Calibrated digital optical spectra for these quasars can be obtained from the SDSS Science Archive Server.

Unified Astronomy Thesaurus concepts: Catalogs (205); Surveys (1671); Quasars (1319); Cosmology (343); Large-scale structure of the universe (902); Observational cosmology (1146)

1. Introduction

The Sloan Digital Sky Survey (SDSS) has a long history of creating and releasing catalogs of quasars for use in cosmology

and studies of quasar physics. SDSS spectroscopically observed 105,783 quasars released between the first (Schneider et al. 2002) and final (Schneider et al. 2010) quasar catalogs of the SDSS legacy programs (SDSS-I/II). When the third iteration of SDSS observations (SDSS-III; Eisenstein et al. 2011) began, the combination of a new spectroscopic instrument, a new focus

³⁰ Independent Researcher.

on quasar programs, extra fibers for spectroscopy, and the discontinuation of imaging observations significantly increased the number of quasars that were observed. Over the course of the SDSS Baryon Oscillation Spectroscopic Survey (BOSS; Dawson et al. 2013) program, three quasar catalogs were released: DR9Q, DR10Q, and DR12Q (Pâris et al. 2012, 2014, 2017), with the final BOSS quasar catalog, DR12Q, containing 297,301 quasars. DR12Q also contained data from external catalogs in other wavelength ranges, multiple redshift estimates, and broad emission-line parameters. DR14Q (Pâris et al. 2018) was the first quasar catalog released as part of the SDSS-IV quasar program, containing 526,356 quasars. In this paper, we release the final quasar catalog of the SDSS-IV quasar program, the extended Baryon Oscillation Spectroscopic Survey (eBOSS; Dawson et al. 2016). This catalog, which we will refer to as DR16Q, contains 920,110 observations of 750,414 quasars. Comparisons of DR16Q to previous quasar catalogs are limited to DR12Q and DR7Q, as these represent the final quasar catalogs accompanying each iteration of SDSS.

One of the primary objectives of eBOSS was to constrain the angular scale of baryon acoustic oscillations (BAOs) in tracers of the distribution of matter (for detection, see Cole et al. 2005; Eisenstein et al. 2005). To achieve the planned precision of 2.8% on the angular diameter distance, $D_A(z)$, and 4.2% on the Hubble parameter, $H(z)$, at $z \sim 1.5$, eBOSS was designed to obtain spectra for a set of $\sim 500,000$ quasars in the redshift range $0.8 < z < 2.2$ (Dawson et al. 2016). This represented more than a fivefold increase in the number of quasars for that redshift range, as compared to the final BOSS quasar catalog, DR12Q. With the final eBOSS observations complete, DR16Q comprises 480,459 quasars within the redshift range $0.8 < z < 2.2$. To constrain BAO measurements at higher redshift, eBOSS also planned to observe 120,000 quasars at $z > 2.1$, increasing the precision on $D_A(z)$ and $H(z)$ from Ly α forest measurements by a factor of 1.44. DR16Q includes 239,081 Ly α quasars, a 25% increase over DR12Q.

While the primary objectives of eBOSS and other SDSS-IV programs informed the target selection for quasars in DR16Q (see Section 2.2), eBOSS quasar catalogs have been used in a number of other recent research studies beyond the eBOSS core programs. These include, but are certainly not limited to, the study of changing-look quasars, which can be used to investigate accretion mechanisms and other quasar physics (Sheng et al. 2020); X-ray studies of the clustering of quasars, which can also give insight into the growth and evolution of supermassive black holes (Powell et al. 2020); studies of the correlation between X-ray and emission-line luminosities (Timlin et al. 2020); studies of quasar outflows in the far-infrared and radio bands via follow-up of optically confirmed quasars (Hall et al. 2019); studies of the correlation of outflow velocities with bolometric luminosity in broad absorption-line (BAL) quasars (Bruni et al. 2019); and studies of the variability in BAL troughs over time (Grier et al. 2016; McGraw et al. 2017). To help facilitate these sorts of quasar studies, DR16Q includes multiple redshift estimates, BAL and damped Ly α (DLA) quasar identifications, and compiled multiwavelength data.

Previous iterations of SDSS quasar catalogs have included redshifts from automated classification pipelines, visual inspections, and principal component analysis (PCA) based on prominent quasar emission lines. In this tradition, DR16Q includes a range of redshift estimates that are characterized by different accuracies, precisions, and levels of homogeneity (see

Section 4 for more details). Most importantly, we have visually inspected 329,130 quasars in the catalog, with 326,535 of these having confident visual classifications and redshifts. Our set of visual inspections also includes the results from a random subsample of 10,000 eBOSS quasar targets. We visually inspected this random subsample and included inspections of different observations of the same quasar to characterize the accuracy and precision of automated redshift algorithms that are also presented in this catalog (again, see Section 4 for more information).

This study is part of a coordinated release of the final eBOSS measurements of BAO and redshift space distortions (RSD) in the clustering of luminous red galaxies (LRGs; $0.6 < z < 1.0$; Bautista et al. 2020; Gil-Marín et al. 2020), emission-line galaxies (ELGs; $0.6 < z < 1.1$; de Mattia et al. 2020; Raichoor et al. 2020; Tamone et al. 2020), and quasars ($0.8 < z < 2.2$; Hou et al. 2020; Neveux et al. 2020). An essential component of these studies is the construction of data catalogs (this catalog; Ross et al. 2020), mock catalogs (Lin et al. 2020; Zhao et al. 2020), and n -body simulations for assessing systematic errors (Rossi et al. 2020; Smith et al. 2020). At the highest redshifts, $z > 2.1$, the coordinated release of final eBOSS measurements includes measurements of BAO in the Ly α forest (du Mas des Bourboux et al. 2020). The cosmological interpretation of these results in combination with the final BOSS results and other probes is found in Alam et al. (2020).

This paper is organized as follows: in Section 2 we summarize the data used to target DR16Q quasars. In Section 3 we outline how we constructed the two different catalog files released as part of DR16Q. In Section 4 we describe the different redshift estimates in DR16Q, their uncertainties, and potential issues for each estimator. In Section 5, we describe the automated algorithms used for identifying and analyzing DLA systems and BAL quasars. In Section 6 we outline the physical properties of the DR16Q quasar sample. In Section 7 we briefly discuss the multiwavelength data included in DR16Q. In Section 8 we describe the quantities included in the DR16Q quasar-only catalog, before concluding in Section 9. We also provide appendices that discuss the precision and accuracy of different redshift estimates for DR16Q quasars, presents some spectra of DR16Q quasars, notes mistakes that we have corrected from previous SDSS quasar catalogs, and details the data model of the DR16Q quasar-only catalog.

2. Survey Outline

In this section we summarize the imaging surveys, target selection procedures, and spectroscopic observations that produced the SDSS-IV/eBOSS quasar sample.

2.1. Imaging Data for Targeting

Three sets of imaging data were used to generate quasar targets for SDSS-IV/eBOSS (Myers et al. 2015). The primary imaging was an updated calibration of SDSS-I/II/III. Additional imaging was incorporated from the Wide-field Infrared Survey Explorer (WISE; Wright et al. 2010) using the custom “unWISE” coadds (Lang et al. 2016). Finally, information on source variability from the Palomar Transient Factory (PTF; Law et al. 2009; Rau et al. 2009) was used to supplement quasar targeting (Palanque-Delabrouille et al. 2016).

SDSS imaging data, in the u , g , r , i , and z photometric bands (Fukugita et al. 1996), was taken at the 2.5 m Sloan telescope

(Gunn et al. 2006) using the 30 $2\text{k} \times 2\text{k}$ CCDs outlined in Gunn et al. (1998). By Data Release 8 (DR8; Aihara et al. 2011), over 14,000 deg 2 of sky was covered by SDSS imaging. SDSS-IV/eBOSS used the same DR8 imaging as SDSS-III/BOSS, but leveraged new photometric calibrations using the “uber-calibration” method of Padmanabhan et al. (2008), updated by Schlafly et al. (2012) to be pinned to PanSTARRS imaging (Kaiser et al. 2010). A full description of this process can be found in Finkbeiner et al. (2016).

The WISE mission (Wright et al. 2010) collected data in four infrared bands: $W1$ (3.4 μm), $W2$ (4.6 μm), $W3$ (12 μm), and $W4$ (22 μm). Lang (2014) used WISE data to create a custom set of coadded “unWISE” images, which were force-photometered at the locations of known SDSS sources by Lang et al. (2016). Due to significant differences in depth between $W1/W2$ and $W3/W4$ data, only $W1$ and $W2$ were used for eBOSS targeting.

PTF imaging was obtained in the Mould R filter and supplemented with SDSS g , as discussed in Ofek et al. (2012). For eBOSS targeting, a custom pipeline was used to coadd individual PTF frames on a timescale of one to four epochs per year. These coadded images were also used to construct a full stack, which was 50% complete to known quasars at a magnitude limit of $g \sim 22.5$. A catalog of sources was extracted from this full stack, and light curves were generated to supplement eBOSS targeting, as detailed in Myers et al. (2015).

2.2. Target Selection

One of the main goals of SDSS-IV/eBOSS was to study dark energy using the BAO method (e.g., Ata et al. 2017). Specifically, the eBOSS quasar sample was designed to achieve a precision on the angular diameter distance, $D_A(z)$, of 2.8% for the redshift range $0.9 < z < 2.2$, and a 4.2% precision in the value of $H(z)$ within that same redshift range for the quasar-quasar autocorrelation. These constraints required a uniformly observed quasar sample density of $>58 \text{ deg}^{-2}$ for the redshift range $0.9 < z < 2.2$. A $z > 2.1$ quasar sample was also targeted to increase constraints on $D_A(z)$ and $H(z)$ in the Ly α forest by $\sim 1.44 \times$ compared to SDSS-III/BOSS (Dawson et al. 2016). eBOSS achieved the targeted precision for the lower redshift range (Hou et al. 2020; Neveux et al. 2020; Smith et al. 2020) and the Ly α forest sample (du Mas des Bourboux et al. 2020). The targeting program to select the eBOSS quasar sample, which is detailed in Myers et al. (2015), is summarized below.

The majority of eBOSS quasars were targeted by a CORE algorithm, which was applied to SDSS SURVEY_PRIMARY point sources with (extinction-corrected) $g < 22$ or $r < 22$. These point sources were passed to the XDQSOz algorithm (Bovy et al. 2012), which imposed a probability of being a quasar at redshifts of $z > 0.9$ of more than 20%. An additional WISE-optical color cut was then applied to further reduce stellar contamination. These two selection criteria led to a quasar sample density of $\sim 70 \text{ deg}^{-2}$. Note that no explicit upper limit on redshift was applied, allowing the CORE sample to also target Ly α -forest quasars.

To constrain cosmological parameters, eBOSS targeted $z > 2.1$ quasars purely as backlights of the Ly α forest, meaning that such quasars could have a heterogeneous angular

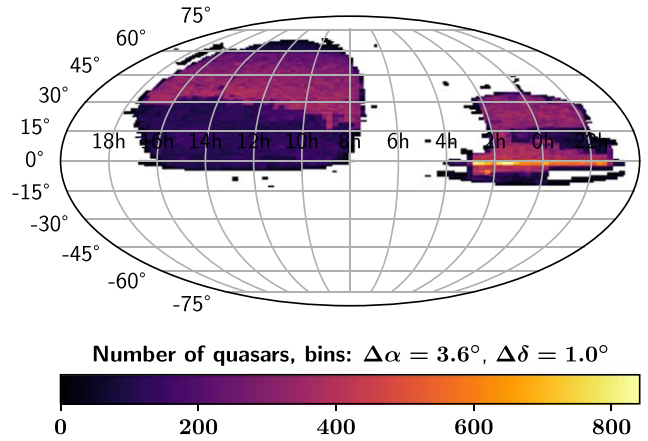


Figure 1. Quasars in DR16Q from SDSS-I/II, BOSS, and eBOSS. R.A. (α) and decl. (δ) are mapped onto a Mollweide projection of the sky.

selection function. The CORE sample was therefore supplemented by three diverse methods designed to increase the yield of Ly α -forest quasars. Objects with $r > 19$ and $g < 22.5$ that displayed quasar-like variability in the PTF light curves discussed in Section 2.1 were included as QSO_PTF targets, increasing the sample density to $\sim 74 \text{ deg}^{-2}$. The $< 1 \text{ deg}^{-2}$ of SDSS point sources that lie within 1'' of a FIRST radio source were included as QSO_EBOSS_FIRST targets. Finally, Ly α quasars that yielded a low signal-to-noise ratio (S/N) spectrum in BOSS were added as QSO_REOBS targets, which increased the on-sky density by between ~ 6 and $\sim 10 \text{ deg}^{-2}$.

Quasars that were targeted by the SDSS-IV subprograms TDSS (detailed in Morganson et al. 2015; MacLeod et al. 2018) and SPIDERS (detailed in Dwelly et al. 2017; Comparat et al. 2020) are also included in DR16Q. The on-sky distribution of DR16Q quasars, which reflects all of the various targeting programs outlined in this subsection, can be seen in Figure 1.

2.3. Spectroscopy

Spectroscopy for SDSS-IV/eBOSS was conducted using the BOSS spectrographs (Smee et al. 2013) on the 2.5 m Sloan Telescope. Two spectrographs each recorded data from 500 fibers on a 2k CCD with square 24 μm pixels and a wavelength range of 3600–10400 Å at a spectral resolution of $\lambda/\Delta\lambda \approx 2000$.

Each calibrated group of 1000 spectra was processed by the BOSS spec1d pipeline (Bolton et al. 2012; see also Section 4.1). Spectra were fit using a variable number of rest-frame-derived PCA templates, which were applied using least-squares minimization to find the 5 best quasar redshifts, 5 best galaxy redshifts, 123 stellar redshifts, and 1 cataclysmic variable star redshift. The fits were then ranked according to the smallest reduced χ^2 (χ_r^2) value. The redshift, object classification, and line identifications were taken from the spectral fit with the lowest χ_r^2 . In the case where two spectral fits had a χ_r^2 difference less than 0.01, a ZWARNING flag was assigned.

DR16Q includes spectra obtained using both the BOSS spectrographs and the SDSS-I/II spectrographs. The cumulative number of observed quasar spectra by campaign is shown

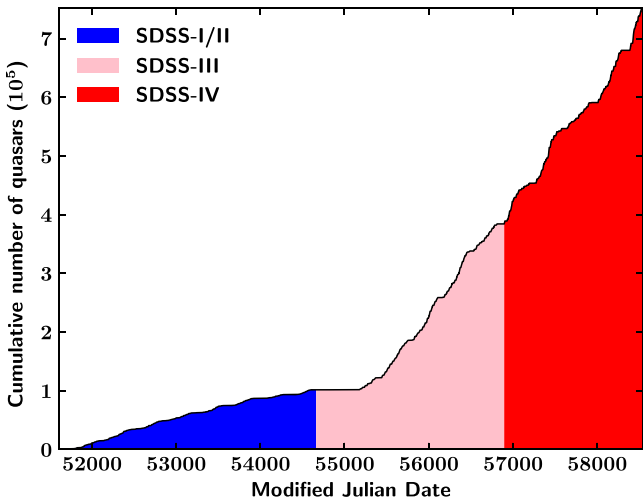


Figure 2. The cumulative number of quasars observed over the four SDSS campaigns. SDSS-I/II is shaded in blue ($MJD < 54,663$), SDSS-III in pink ($54,663 \leq MJD < 56,898$), and SDSS-IV in red ($56,898 \leq MJD < 58,543$). Quasars observed multiple times were included based on their first spectroscopic observation. DR16Q includes 750,414 confirmed quasars. Flat regions of the plot indicate periods of shutdown.

in Figure 2. Wavelength limits for the spectra differ between the two set-ups, with SDSS-I/II spectra covering 3800–9100 Å (see Smee et al. 2013).

3. Construction of the Catalog

As DR16Q represents the final SDSS-IV quasar catalog, it contains all quasars observed as part of eBOSS, TDSS, and SPIDERS. Additionally, like the catalog of Pâris et al. (2018, henceforth DR14Q), quasars observed in SDSS-I/II, and SDSS-III/BOSS have been included. Quasars presented in Schneider et al. (2010, henceforth DR7Q) and Pâris et al. (2017, henceforth DR12Q) that did not have an eBOSS observation were added via coordinate matching, as detailed in Section 3.1. Due to quasar identification errors, quasars in DR14Q without a match in DR16Q were not included in DR16Q (see Appendix C for details). The python code for generating DR16Q is available publicly.³¹

3.1. Definition of the Superset

The DR16Q superset was constructed from `spAll-v5_13_0.fits` (henceforth “the `spAll` file”), the file of all SDSS-III/IV observations generated by version `v5_13_0` of the SDSS spectroscopic pipeline.³² Any observation in the `spAll` file that has a bit flagged that is recorded in the columns listed in Table 1 was included in the DR16Q superset.

As the `spAll` file does not include observations from SDSS-I/II, quasars from DR7Q without an eBOSS reobservation were added to the DR16Q superset. Additionally, some quasars appearing in DR12Q were serendipitous identifications and did not have the bits set from Table 1. DR7Q and DR12Q were coordinate-matched with a $0.^{\circ}5$ radius to the superset, and missing objects were added. If a quasar already appeared in the

superset, only the redshift and spectroscopic identifiers (plate, MJD, and fiber ID) were added to the SDSS-III/IV record. Known astrometric errors in DR12Q were corrected before coordinates were matched. The DR7Q and DR12Q quasars were added to the superset after the winnowing algorithm outlined in Section 3.2 was applied, as any objects appearing in DR7Q and DR12Q had previously been visually confirmed to be confident quasars. For quasars included in both DR7Q and DR12Q, only the DR7Q observation was propagated to this catalog superset.

The superset contains 1,440,615 observations of quasars, stars, and galaxies that were all targeted as quasars (or appeared in previous quasar catalogs).

3.2. Automated Classification

Spectra flagged as in Table 1 were selected from the `spAll` file and passed through a modified version of a classification scheme that first appeared in Dawson et al. (2016). The “top five” classifications (those with the five lowest χ^2 ; see Section 2.3) are used in the following decision tree (in order) to set the value of the `AUTOCLASS_DR14Q` field:

1. If the best model fit for the spectrum is STAR, the spectrum is classified as a STAR.
2. If the best model fit for the spectrum is GALAXY and $Z_{\text{pipe}} < 1$, then the spectrum is classified as a GALAXY.
3. If the best model fit for the spectrum is GALAXY, $Z_{\text{pipe}} \geq 1$, and at least one other fit is GALAXY, then the spectrum is classified as a GALAXY.
4. If the best model fit for the spectrum is QSO and two or more other model fits are STAR, then the spectrum is classified as a STAR.
5. If the best model fit for the spectrum is QSO, fewer than two other model fits are STAR, and $Z_{\text{WARNING}} = 0$, the spectrum is classified as a QSO.
6. If a spectrum meets none of these criteria, it is selected for visual inspection (`AUTOCLASS_DR14Q = VI`).

Each individual spectrum was classified using this schema, and afterwards, any object that had an initial classification of QSO and $Z_{\text{pipe}} > 3.5$ was reclassified for visual inspection (`AUTOCLASS_DR14Q = VI`). This algorithm flagged $\sim 6\%$ of the superset ($\sim 87,000$ spectra) for visual inspection. To reduce duplication of effort, we only visually inspected spectra taken after MJD 57905, the last date of inspections for DR14Q. This reduced our flagged percentage to $\sim 1.5\%$, or 20,508 spectra.

To further reduce the number of visual inspections, the QuasarNET algorithm (Busca & Balland 2018) was applied. QuasarNET produces a binary quasar flag and a redshift, which we designated `IS_QSO_QN` and `Z_QN`, respectively. We used the results stored in `AUTOCLASS_DR14Q` to reclassify objects based on confident QuasarNET classifications, recording the output in `AUTOCLASS_PQN`. `AUTOCLASS_PQN` retained the same classification as `AUTOCLASS_DR14Q` for all cases but one: if `AUTOCLASS_DR14Q` was VI, `IS_QSO_QN` = 1, and $Z_{\text{QN}} < 2.0$, then `AUTOCLASS_PQN` was changed to QSO. Applying QuasarNET led to a reduction in the number of spectra to inspect to $\sim 0.6\%$ (8581 spectra). Finally, objects were removed from the superset where the `ZWARNING`³³ field had one or more of the following flags set:

³¹ <https://github.com/bradlyke/dr16q>

³² https://data.sdss.org/datamodel/files/BOSS_SPECTRO_REDUX/RUN2D/spAll.html

³³ www.sdss.org/dr16/algorithms/bitmasks/#ZWARNING

Table 1
Targeting Bit Parameters

Bit	Selection	Bit	Selection	Bit	Selection	Bit	Selection
BOSS_TARGET1							
10	QSO_CORE (1)	11	QSO_BONUS (1)	12	QSO_KNOWN_MIDZ (1)	13	QSO_KNOWN_LOHIZ (1)
14	QSO_NN (1)	15	QSO_UKIDSS (1)	16	QSO_KDE_COADD (1)	17	QSO_LIKE (1)
18	QSO_FIRST_BOSS (1)	19	QSO_KDE (1)	40	QSO_CORE_MAIN (1)	41	QSO_BONUS_MAIN (1)
42	QSO_CORE_ED (1)	43	QSO_CORE_LIKE (1)	44	QSO_KNOWN_SUPPZ (1)		
EBOSS_TARGET0							
10	QSO_EBOSS_CORE (5)	11	QSO_PTF (5)	12	QSO_REOBS (5)	13	QSO_EBOSS_KDE (5)
14	QSO_EBOSS_FIRST (5)	15	QSO_BAD_BOSS (5)	16	QSO_BOSS_TARGET (5)	17	QSO_SDSS_TARGET (5)
18	QSO_KNOWN (5)	20	SPIDERS_RASS_AGN (6)	22	SPIDERS_ERASS_AGN (6)	30	TDSS_A (7)
31	TDSS_FES_DE (8)	33	TDSS_FES_NQHISN (8)	34	TDSS_FES_MGII (8)	35	TDSS_FES_VARBAL (8)
40	SEQUELS_PTF_VARIABLE						
EBOSS_TARGET1							
9	QSO1_VAR_S82 (9)	10	QSO1_EBOSS_CORE (5)	11	QSO1_PTF (5)	12	QSO1_REOBS (5)
13	QSO1_EBOSS_KDE (5)	14	QSO1_EBOSS_FIRST (5)	15	QSO1_BAD_BOSS (5)	16	QSO_BOSS_TARGET (5)
17	QSO_SDSS_TARGET (5)	18	QSO_KNOWN (5)	30	TDSS_TARGET (7), (8), (10)	31	SPIDERS_TARGET (6), (10)
EBOSS_TARGET2							
0	SPIDERS_RASS_AGN (6)	2	SPIDERS_ERASS_AGN (6)	4	SPIDERS_XMMSL_AGN (6)	20	TDSS_A (7)
21	TDSS_FES_DE (8)	23	TDSS_FES_NQHISN (8)	24	TDSS_DES_MGII (8)	25	TDSS_FES_VARBAL (8)
26	TDSS_B (7)	27	TDSS_FES_HYPQSO (8)	31	TDSS_CP (8)	32	S82X_TILE1 (10)
33	S82X_TILE2 (10)	34	S82X_TILE3 (10)	50	S82X_BRIGHT_TARGET (10)	51	S82X_XMM_TARGET (10)
52	S82X_WISE_TARGET (10)			53	S82X_SACLAY_VAR_TARGET (10)		
54	S82X_SACLAY_BDT_TARGET (10)			55	S82X_SACLAY_HIZ_TARGET (10)		
56	S82X_RICHARDS15_PHOTOQSO_TARGET (10)			57	S82X_PETERS15_COLORVAR_TARGET (10)		
58	S82X_LSSTZ4_TARGET (10)			59	S82X_UNWISE_TARGET (10)		
60	S82X_GTRADMZ4_TARGET (10)			61	S82X_CLAGN1_TARGET (10)		
62	S82X_CLAGN2_TARGET (10)						
ANCILLARY_TARGET1							
6	BLAZGVAR (2)	7	BLAZR (2)	8	BLAZXR (2)	9	BLAZXRSL (2)
10	BLAZXRVAR (2)	11	XMMBRIGHT (2)	12	XMMGRIZ (2)	13	XMMHR (2)
14	XMMRED (2)	15	FBQSBAL (2)	16	LBQSBAL (2)	17	ODDBAL (2)
18	OTBAL (2)	19	PREVBAL (2)	20	VARBAL (2)	22	QSO_AAL (2)
23	QSO_AALS (2)	24	QSO_IAL (2)	25	QSO_RADIO (2)	26	QSO_RADIO_AAL (2)
27	QSO_RADIO_IAL (2)	28	QSO_NOAALS (2)	29	QSO_GRI (2)	30	QSO_HIZ (2)
31	QSO_RIZ (2)	50	BLAZGRFLAT (2)	51	BLAZGRQSO (2)	52	BLAZGX (2)
53	BLAZGXQSO (2)	54	BLAZGXR (2)	55	BLAZXR (2)	58	CXOBRIGHT (2)
59	CXORED (2)						
ANCILLARY_TARGET2							
0	HIZQSO82 (2)	1	CXOREDHIZQSOIR (2)	2	KQSO_BOSS (2)	3	QSO_VAR (2)
4	QSO_VAR_FPG (2)	5	RADIO_2LOBE_QSO (2)	7	QSO_SUPPZ (2)	8	QSO_VAR_SDSS (2)
9	QSO_WISE_SUPP (3)	10	QSO_WISE_FULL_SKY (4)	13	DISKEMITTER_REPEAT (4)	14	WISE_BOSS_QSO (4)
15	QSO_XD_KDE_PAIR (4)	24	TDSS_PILOT (4)	25	SPIDERS_PILOT (4)	26	TDSS_SPIDERS_PILOT (4)
27	QSO_VAR_LF (4)	31	QSO_EBOSS_W3 ADM (4)	32	XMM_PRIME (4)	33	XMM_SECONDS (4)
53	SEQUELS_TARGET (4)	54	RM_TILE1 (4)	55	RM_TILE2 (4)	56	QSO_DEEP (4)

References. (1) Ross et al. (2012), (2) Dawson et al. (2013), (3) Ahn et al. (2014), (4) Alam et al. (2015), (5) Myers et al. (2015), (6) Dwelly et al. (2017), (7) Morganson et al. (2015), (8) MacLeod et al. (2018), (9) Palanque-Delabrouille et al. (2016), (10) Abolfathi et al. (2018).

UNPLUGGED, SKY, LITTLE_COVERAGE, BAD_TARGET, or NODATA.

To characterize the accuracy of our classification scheme, the SDSS-III/SEQUELS data set (see Section 5.1 of Myers et al. 2015) was used as “truth” to calculate the sample

completeness via

$$\text{Comp} = \frac{N_{pq} + N_{vq}}{N_{tq}}, \quad (1)$$

where N_{pq} is the number of quasars correctly classified as QSO by our schema, N_{vq} is the number of quasars identified during visual inspections, and N_{tq} is the total number of quasars in the catalog. We also calculated the sample contamination via

$$\text{Contam} = \frac{N_{\text{nq}}}{N_{\text{tq}} + N_{\text{nq}}}, \quad (2)$$

where N_{nq} is the number of spectra incorrectly classified as quasar spectra and N_{tq} is as in Equation (1). We calculated a completeness of 99.2% and a contamination of 0.5%. Due to increased observation time and subsequent higher S/Ns for these spectra, the BOSS SEQUELS set is not necessarily a good indicator of the spectral quality throughout eBOSS.

3.3. Random eBOSS Visual Inspections

To better characterize the eBOSS spectral pipeline, a random subsample of 10,000 eBOSS spectra from the DR16Q superset was selected. This subsample consisted of objects from the eBOSS CORE set and non-CORE objects with a pipeline redshift greater than 1.8. This subsample was visually inspected to check whether the pipeline correctly classified the spectrum and, in the case of quasar spectra, assigned an accurate redshift (“accurate” being defined as $\Delta v \leq 3000 \text{ km s}^{-1}$; see also Section 4.6). Whether the pipeline’s classification (and redshift) was correct is recorded in DR16Q in the column PIPE_CORR_10K. If the pipeline was correct, Z_10K was set to the pipeline redshift, and the pipeline’s determination of a quasar classification was retained.

If the pipeline did not correctly classify the spectrum, or a quasar redshift was significantly wrong ($\Delta v > 3000 \text{ km s}^{-1}$), the classification was corrected and quasar redshifts were recalculated as detailed in Section 3.4. These data are recorded in DR16Q in columns IS_QSO_10K for classification, Z_10K for the redshift, and Z_CONF_10K for the redshift confidence in the case of quasars. Equation (1) was applied to this set, producing a completeness of 99.8%. Some of the random subsample of 10,000 eBOSS spectra with a low S/N were classified as quasars by the DR14Q visual inspection team but were reclassified as non-quasars by the DR16Q team. Applying Equation (2) and using DR14Q classifications for such cases produced an estimated contamination of 0.3%. Using DR16Q classifications for such cases produced an estimated contamination of 1.3%.

3.4. Visual Inspection in eBOSS

In past SDSS visually inspected catalogs, such as DR7Q (Schneider et al. 2010) and DR12Q (Páris et al. 2017), the number of quasar candidates was small enough for each spectrum to be visually inspected. In eBOSS the number of observations rose precipitously, so, for DR16Q, we only visually inspected objects as outlined in Section 3.2. As in DR14Q, objects selected for visual inspection were reclassified and quasar redshifts were corrected where needed. Spectra that were not quasars upon visual inspection, or that had a very low S/N, were classified as “non-quasars” and did not have their redshifts corrected. These appear in the superset with CLASS_PERSON = 4 (GALAXY), and have Z_VI = -1. The numeric system used to classify spectra in DR16Q is shown in Table 2. This system is similar to that used in DR12Q, but the

Table 2
Visual Inspection Classifications, which Appear in the CLASS_PERSON Column of DR16Q

Value	Object Type	Value	Object Type
0	Not inspected	1	Star
3	Quasar	4	Galaxy
30	BAL quasar	50	Blazar(?)

(unused) value of 2 was removed for DR16Q and a new value of 50 was added to indicate potential blazars.

Any spectra flagged for visual inspection in DR16Q were classified as a “non-quasar” if the noise spectrum was greater than the continuum everywhere and no more than one emission-line peak rose above the noise level. If two emission-line peaks could be positively identified, the object was classified as a quasar and given a corrected, “visual inspection” redshift. In a few cases, a single evident emission-line peak could be questionably identified. Where this was true, the redshift was corrected using that emission line, the object was classified as a quasar, but the confidence rating for the redshift (Z_CONF; described below) was set to 1. During visual inspection, we identified four spectra with high flux, continua matching an archetypal quasar continuum shape, and no identifiable absorption or emission features. These spectra were marked as possible blazars; they were assigned a CLASS_PERSON value of 50 and a redshift of -999.

Where emission-line peaks (or other features) could be identified, a new redshift was calculated by using the peak (or feature) wavelength for the following emission lines in priority order: Mg II $\lambda 2799$, C IV $\lambda 1549$, C III] $\lambda 1908$, [O III] $\lambda 5007$, [O II] $\lambda 3728$, and Lyman break $\lambda 912$. A confidence rating for these redshifts was recorded in the column Z_CONF, with 0 being the lowest and 3 being the highest confidence (a value of -1 indicates the object was not visually inspected). Spectra with one questionable emission line were given a confidence rating of 1. Spectra with two or more lines identified based on pipeline locations were given a confidence rating of 2. In all cases, visual inspection redshifts were calculated to three decimal places. If the visual inspection redshift agreed with the pipeline, the visual inspection redshift was set to the pipeline redshift.

Unlike DR12Q, spectra of general interest such as those of DLA systems and BAL quasars were not flagged as part of the visual inspection process. Instead, DLAs and BALs were identified via algorithm, as described in Section 5.

As the SDSS classification pipeline changed substantially between DR14Q and DR16Q, DR16Q only includes visual inspection information from DR14Q for objects that were in the DR16Q superset. Additionally, objects in DR16Q with $z > 5$ and SOURCE_Z = PIPE should be considered suspect, as they sometimes have misleading spectroscopic reductions or classifications. Users should carefully reinspect such objects prior to using them for scientific analyses.

3.5. Duplicate Observation Removal

Some SDSS-IV/eBOSS quasar targets were part of multi-epoch campaigns (e.g., Reverberation Mapping; Shen et al. 2015; TDSS; Morganson et al. 2015; MacLeod et al. 2018). Additionally, many targets observed in previous SDSS campaigns were reobserved in eBOSS. To reduce the superset

of observations to objects, we employed the following algorithm:

1. The superset catalog was coordinate-matched to itself with a maximum matching radius of $0.^{\circ}5$, and self-matches were removed.
2. For objects that had at least one visual inspection, we selected the observation with the highest VI confidence rating.
3. If all of the confidence ratings were the same, or none of the observations had a visual inspection, we selected the observation with the highest SN_MEDIAN_ALL value.

The SN_MEDIAN_ALL value represents the median S/N across all good pixels in a spectrum. Primary observations were marked with a 1 in the PRIM_REC column of the DR16Q superset. For nonprimary observations, the spectroscopic plate, modified Julian date, fiber ID number, and spectroscopic instrument (SDSS or BOSS) were recorded in the fields of the primary observation marked PLATE_DUPLICATE, MJD_DUPLICATE, FIBERID_DUPLICATE, and SPECTRO_DUPLICATE, respectively. The number of duplicate observations for each spectroscopic set-up was also tallied and recorded in NSPEC_SDSS and NSPEC_BOSS. The column NSPEC records the total number of duplicate observations. All duplicate observations are included as individual records in the DR16Q superset, but only quasars with PRIM_REC set to 1 were used to create the DR16Q quasar-only catalog.

3.6. Classification Results

DR16Q primarily contains data from eBOSS, but quasars appearing in DR7Q and DR12Q were also added (to both the DR16Q superset and the quasar-only catalog) if they did not already appear in the DR16Q superset. Due to the varied sources for the superset records, a more robust final classification for quasars was needed. A new column titled IS_QSO_FINAL was created that can take integer values from -2 to 2 . In brief, quasar spectra have a value of 1 and questionable quasar spectra a value of 2 . All values of 0 or less denote non-quasars. We developed a new algorithm to merge all of the independent, confident quasar classification sources into a final value. This final classification was generated by the following algorithm after the removal of duplicate observations:

1. If AUTOCLASS_PQN was QSO, the object is a quasar and IS_QSO_FINAL = 1.
(a) However, if CLASS_PERSON = 1 or 4 and Z_CONF ≥ 2 , the object was not a quasar and IS_QSO_FINAL = -2 .
2. If Z_VI or Z_10K = -999 , these are possible blazars and IS_QSO_FINAL = 1.
3. If AUTOCLASS_PQN = UNK, CLASS_PERSON = 3 or 30, and Z_CONF ≥ 2 , the object is a quasar and IS_QSO_FINAL = 1.
(a) If the above is true, but Z_CONF = 1, then the classification as a quasar is questionable, but included. We set IS_QSO_FINAL = 2. There were 69 objects in this subset.
4. If SOURCE_Z is DR12QV, DR7QV_SCH, or DR6Q_HW, the object was visually confirmed to be a quasar in a previous catalog, and we set IS_QSO_FINAL = 1.

Table 3
Classification Results

Superset Numbers	
Observations from SDSS-I/II	73,325
Observations from SDSS-III/IV	1,367,290
Total observations in Superset	1,440,615
Quasar observations in Superset	920,110
Duplicate quasar observations in DR16Q	199,904
Quasar-only Numbers	
Quasars with automated redshift only	341,622
Quasars with a visual inspection redshift	408,792
Total DR16Q quasars	750,414

5. If RANDOM_SELECT = 1 and IS_QSO_10K = 1, the object is visually confirmed to be a quasar, and we set IS_QSO_FINAL = 1.
6. If IS_QSO_DR12Q or IS_QSO_DR7Q = 1, we set IS_QSO_FINAL = 1. This subset occurred when an object had an eBOSS primary observation and a duplicate DR12Q or DR7Q observation.
7. If AUTOCLASS_PQN = VI, CLASS_PERSON = 3, 30, or 50, and Z_CONF ≥ 2 , then we set IS_QSO_FINAL = 1.
(a) However, if this last condition is true except Z_CONF = 1, the object is questionably a quasar, and we set IS_QSO_FINAL = 2. There were 670 objects in this subset.

AUTOCLASS_PQN, CLASS_PERSON, Z_VI, Z_10K, SOURCE_Z, RANDOM_SELECT, and the various IS_QSO_YYY columns are described in detail in Section 8. Once the IS_QSO_FINAL column was populated in the DR16Q superset, only objects with IS_QSO_FINAL > 0 were selected for the quasar-only catalog.

Two special cases existed after assigning classifications: first, an object classified as a quasar by the algorithm in Section 3.2 that had a low-confidence visual inspection classifying it as a non-quasar. Such objects were left in the quasar-only catalog but are possible contaminants. The second is an object classified as a quasar by a low-confidence visual inspection that was classified as a non-quasar by the automated algorithm. Such objects were removed and represent possible lost quasars. In other words, confident visual inspection classifications would override automated classifications, but low-confidence visual classifications would not.

Table 3 lists the number of observations and objects appearing in both the DR16Q superset and the DR16Q quasar-only catalog.

4. Redshift Estimates

A homogeneously defined set of quasar redshifts is integral to the eBOSS mission of characterizing large-scale structure. Alternate redshift estimates, however, may be more useful for other science needs. We have therefore chosen to include a number of different redshift estimates in DR16Q, which we detail in this section.

4.1. Automated Redshifts

DR16Q includes automated classifications and redshifts determined by version v5_13_0 of the SDSS spectroscopic pipeline. Observed spectra are fit by a set of models and templates that are detailed in Bolton et al. (2012). Quasar models are first fit by searching over redshifts binned in redshift space where bins are separated by four SDSS pixels in constant log-lambda spacing. The five models with the lowest χ^2 are then fit to every pixel. These “top five” quasar fits are then compared, using reduced χ^2 values, to the best 5 model fits for galaxies, 123 fits to stellar templates, and a fit to a cataclysmic variable template. Dubious pixels in spectra can be masked before fitting, but good spectra typically retain ~ 4500 pixels to fit. Quasar models include four eigenspectra components derived from BOSS reobservations of 568 SDSS DR5 quasars and a quadratic polynomial. In the version of the pipeline used to construct DR16Q, quasar models were optimized for BOSS, which targeted Ly α forest quasars at about $z \geq 2.2$. In particular, the pipeline has trouble confidently distinguishing redshifts in the range $1.0 \leq z \leq 2.0$ for which the strong [O III] and Ly α emission lines are not present in the eBOSS spectrum.

To check the quality of the pipeline classifications and redshifts, we compared the visual inspection redshifts derived from our random set of 10,000 superset spectra (Z_{10K} ; see Section 3.3) to their pipeline values (Z_{PIPE}) for eBOSS CORE targets. Using a value of $\Delta v > 3000 \text{ km s}^{-1}$ to define an inaccurate pipeline redshift (see also Section 4.6), we found that 2.1% of the pipeline redshifts were inaccurate. This represented 154 catastrophic failures out of 7254 quasars. Further, the vast majority (130) of these catastrophes were highly inaccurate, where $\Delta v \geq 10,000 \text{ km s}^{-1}$.

4.2. QuasarNET Redshifts

As discussed in Section 3.2, we used redshifts from the QuasarNET³⁴ algorithm to help determine which quasars to visually inspect. We record this redshift in DR16Q as Z_{QN} . For more information on QuasarNET, we refer the reader to Busca & Balland (2018).

4.3. Visual Inspection Redshifts

DR16Q includes the visually inspected redshifts for quasars that appeared in DR7Q or DR12Q in the $Z_{\text{DR7Q_SCH}}$ and Z_{DR12Q} columns. We also include the redshifts from Hewett & Wild (2010), where available, in the field $Z_{\text{DR6Q_HW}}$, as they are formally in the Hewett and Wild paper and have been used in some of our companion papers. We are conscious that a large body of work uses the updated DR7Q Hewett and Wild redshifts included in the ancillary columns of the value-added catalog detailed in Shen et al. (2011). We include these redshifts in their own column, $Z_{\text{DR7Q_HW}}$, for completeness. To conform with other reported redshifts, we do not include the Shen et al. (2011) redshift errors in DR16Q.³⁵ For objects inspected after DR12Q, the visual inspections are included in the field Z_{VI} . Redshifts for quasars found during the random visual inspection (see Section 3.3) are recorded in the column Z_{10K} . While some of these values may overlap, we include each separately, as data reduction techniques may have

changed between observations. In all cases, the field $SOURCE_Z$ records the origin of the primary redshift estimate, and the estimate itself is recorded in Z (as detailed in Section 4.5).

4.4. PCA Redshift and Emission-line Redshifts

In the tradition of previous BOSS and eBOSS quasar catalogs, DR16Q includes a redshift generated by principal component analysis (PCA), using the `redvsblue` algorithm.³⁶ These redshifts are recorded in the Z_{PCA} field of DR16Q.

In fitting the spectra, the `redvsblue` algorithm uses the same four PCA eigenvectors as the SDSS spectroscopic pipeline and includes a second-degree polynomial as a broadband term. Unlike the SDSS pipeline, `redvsblue` uses all pixels within the observed wavelength range 3600–10000 Å, regardless of whether they would be masked by the pipeline. The `redvsblue` algorithm is also not limited to the pipeline redshift range of $0 \leq Z_{\text{pipe}} \leq 7$.

For quasars in the DR16Q quasar-only sample, we stacked all spectra that did not have the `ZWARNING`³⁷ flags `SKY`, `LITTLE_COVERAGE`, `UNPLUGGED`, `BAD_TARGET` or `NODATA` set, before assigning a PCA redshift. Spectra are “stacked” by matching them in log-lambda space and taking an error-weighted average of the flux density at each point. For data appearing in the DR16Q superset, only the best observation was used. For both the DR16Q quasar-only catalog and the superset, the `redvsblue` algorithm corrected all observed spectra for Galactic extinction using the dust map of Schlegel et al. (1998). The algorithm also corrected the model PCA eigenvectors for Ly α transmission evolution using parameters from Calura et al. (2012). We used the primary DR16Q redshift (Z), with a flat prior of $\Delta v \pm 10,000 \text{ km s}^{-1}$, to seed an initial redshift estimate. In addition to the full-spectrum PCA redshift (Z_{PCA}), we independently computed six emission-line redshifts (H α , H β , Mg II, C III], C IV, and Ly α) using the same prior on the primary redshift (Z) used to calculate Z_{PCA} but not using Z_{PCA} itself.³⁸ We include these redshifts in DR16Q when the emission line of interest is in the observed frame of the spectrum. A distinct PCA redshift was used in the Ly α forest clustering catalogs. This redshift, recorded in the column Z_{LYAWG} masks the Ly α emission line and potential forest before generating a redshift. More details about this redshift can be found in du Mas des Bourboux et al. (2020).

Some of the 750,414 sources in the DR16Q quasar-only sample did not yield good PCA redshifts. These included 12,412 quasars where Z_{PIPE} disagreed with Z_{QN} by more than $10,000 \text{ km s}^{-1}$; 1085 quasars that did not have an SDSS identifier (`THING_ID`³⁹ = −1), so could not be stacked for the quasar-only catalog; 4 quasars with $Z = -999$ (possible blazars); and 444 that had outlier spectra that `redvsblue` could not fit reliably. In addition, there are 11 quasars that have $Z_{\text{PCA}} < 0$. In total, 665,612 quasars in the quasar-only catalog yielded reliable PCA redshifts. The DR16Q superset contains 920,109 quasars with $Z_{\text{PCA}} > 0$. These PCA

³⁴ <https://github.com/ngbusca/QuasarNET>

³⁵ See columns 143 and 144 at http://das.sdss.org/va/qso_properties_dr7/dr7.htm.

³⁶ <https://github.com/londumas/redvsblue>

³⁷ www.sdss.org/dr16/algorithms/bitmasks/#ZWARNING

³⁸ We use “PCA redshift” to denote a redshift not tied to a single emission line. Redshifts derived from a single emission line are referred to as “emission-line redshifts.”

³⁹ <http://www.sdss.org/dr16/algorithms/resolve/>

redshifts represent a sample with homogeneous statistical and systematic errors.

4.5. Selection of the “Primary” Redshift

DR16Q includes many different quasar redshift estimates. We select a “primary” redshift (similar to the “best” redshift in DR14Q) for each object from, most preferably, the available visual inspection redshifts, or, alternatively, the SDSS automated pipeline redshift. The columns Z and $SOURCE_Z$ record this primary redshift and from which column it was selected. See Section 4.3 for more information on the available visual inspection redshifts.

For objects that have a redshift in columns Z_{VI} or Z_{10K} and a confidence (Z_{CONF} or Z_{CONF_10K}) of ≥ 2 , Z records the corresponding redshift and $SOURCE_Z$ is set to VI . Otherwise, if an object has a redshift in columns Z_{DR6Q_HW} or Z_{DR7Q_SCH} , these values are used (with Z_{DR6Q_HW} overriding Z_{DR7Q_SCH}), and $SOURCE_Z$ is set to $DR6Q_HW$ or $DR7QV_SCH$. As the Z_{DR7Q_HW} redshifts did not formally appear in the Shen et al. (2011) paper, these values are not used to populate the Z column. If no other visual inspection redshift is populated, then Z_{DR12Q} is used (and $SOURCE_Z$ is set to $DR12QV$). For objects with $DR12Q$ redshifts, only the visual inspection redshifts are recorded; $DR12Q$ pipeline redshifts are not included. In the absence of any of these visual inspection redshifts, Z is populated with the automated pipeline redshift (and $SOURCE_Z$ is set to $PIPE$).

The PCA and QuasarNET redshifts are included in their own columns in DR16Q but were not used to inform the Z column. Given the heterogeneous source information that is propagated into the Z column, we expect Z to represent the least-biased redshift estimator, but with a high variance. For analyses that require a homogeneous redshift over a large ensemble, we recommend Z_{PCA} . We ourselves use Z_{PCA} in this paper as a redshift prior for calculating absolute i -band magnitudes, and for finding DLAs and BALs (Section 5).

4.6. Comparison of Redshift Values

The number and complexity of physical processes that can affect the spectrum of a quasar make it difficult to precisely and accurately disentangle a “systemic” redshift (i.e., as a meaningful indicator of distance) from measured redshifts. Indeed, quasar spectra contain broad emission lines due to the rotating gas located around the central black hole that are subject to matter outflows around the accretion disk. These astrophysical processes frequently give rise to systematic offsets when measuring redshifts. To investigate the systematic shifts associated with the automated and emission-line redshifts (Z_{pipe} , Z_{PCA} , and Z_{line}), we used the Reverberation Mapping program (Shen et al. 2015) to compare the eBOSS redshifts to these “systemic” redshifts obtained from coadded spectra of 849 confirmed quasars where $0.1 < z < 4.5$. Shen et al. (2016) measured the velocity shifts of quasar emission-line peaks compared to stellar absorption lines from the host galaxy of individual quasars. These stellar features correspond to absorption in the host galaxy which is not affected by contaminating physical processes providing reliable “systemic” velocity measurements. Thus, the “systemic” redshifts are henceforth referred to as “host” redshifts. We discarded the first

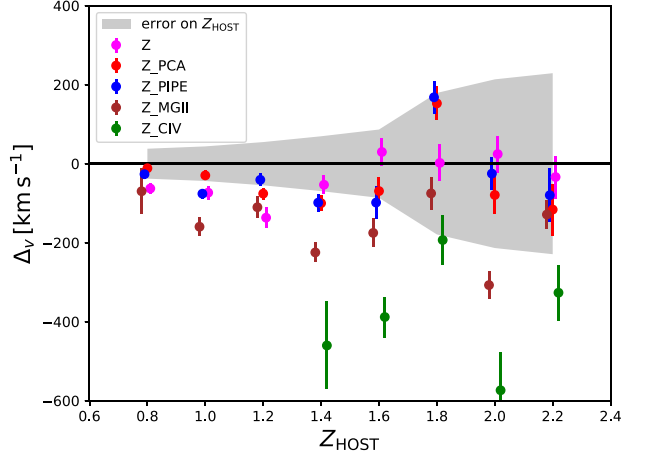


Figure 3. The velocity difference between measured redshift and the host redshift, Z_{HOST} , as a function of Z_{HOST} for different redshift tracers. The gray area represents the 1σ uncertainty for Z_{HOST} . The velocity difference is defined in Equation (3), though the redshift difference is used in place of the absolute redshift difference to characterize systematic red- or blueshifting of the velocity difference. “Host” does not imply this is an unbiased estimate of the redshift, but an estimate derived from the host galaxies of quasars at low redshift.

year of observations, to match the eBOSS observation time, and kept only quasars in the redshift range $0.8 < z < 2.2$.

We define the velocity difference for redshifts as

$$\Delta v = c \times \frac{|Z_c - Z_T|}{1 + Z_T}, \quad (3)$$

where Z_c is the redshift under comparison, c is the speed of light, and Z_T is the redshift baseline used for comparison. In Figure 3, Z_{HOST} is used for Z_T , which is compared to various redshifts available in the catalog as a function of this host redshift. Only Z (the “primary” redshift detailed in Section 4.5), Z_{PCA} , and Z_{pipe} show systematic shifts that are less than the uncertainty on the host redshift itself. Our study also confirmed that $Z_{Mg\text{ II}}$ is the least-biased broad emission-line redshift estimate as previously reported in, e.g., Shen et al. (2016).

In addition to systematic uncertainty, each measured redshift contains a statistical precision that we can estimate using duplicate observations. These duplicate observations are made possible in overlapping plates when unused fibers are assigned to quasars with previous observations. Figure 4 shows the offset in velocity between two redshift measurements of the same quasar. The statistical precision of Z_{PCA} and Z_{pipe} shows a similar behavior with no significant redshift dependence for the eBOSS redshift range and shows a statistical uncertainty of $\sim 300 \text{ km s}^{-1}$. A more detailed discussion of statistical uncertainties in Z_{PCA} and Z_{pipe} can be found in Appendix A.

For the catalog as a whole, we define quasars in DR16Q as being a “catastrophic failure” if they have a velocity difference from a reference redshift of $\Delta v > 3000 \text{ km s}^{-1}$. As the Shen et al. (2015) quasar sample is much smaller than DR16Q, we do not have “host” redshifts to calculate catastrophic failures for the entire catalog. We define a different redshift, Z_{PCA} , as Z_T for comparing the catastrophic failure rate of redshifts from various sources in the Z column. For a detailed discussion of the use of Z_{PCA} in the clustering catalog, see Ross et al. (2020). The comparisons of the various sources to Z_{PCA} can be found in Table 4, which also includes a comparison to Z for a “full

Table 4
Velocity Differences by SOURCE_Z

SOURCE_Z	Sample Size	Acceptable Δv $\Delta v \leq 3000 \text{ km s}^{-1}$	Catastrophic Failures $\Delta v > 3000 \text{ km s}^{-1}$	Catastrophic Failure Rate	Median Δv km s^{-1}	MAD Δv km s^{-1}
VI	319,518	314,392	5126	1.60%	216.2	165.5
PIPE	355,948	354,713	1235	0.35%	48.5	33.9
DR7Q_SCH	11,124	11,002	122	1.10%	148.5	115.4
DR6Q_HW	63,133	62,641	492	0.78%	130.5	87.8
DR12Q	18	18	0	0.00%	170.0	123.1
TOTAL	749,741	742,766	6975	0.93%	93.0	73.5

Note. MAD Δv is the median absolute deviation of the velocity difference.

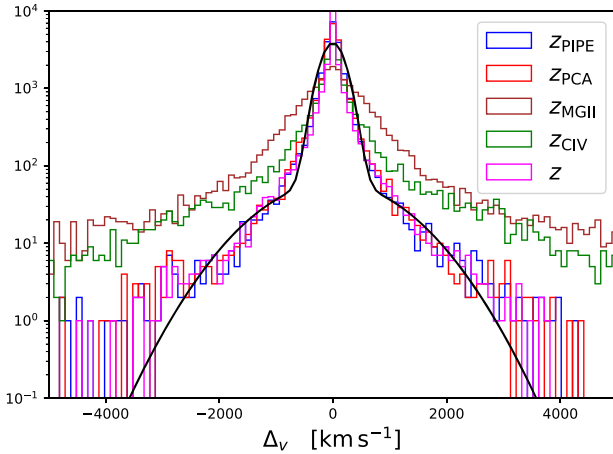


Figure 4. The distribution of the velocity difference for the same redshift tracers seen in Figure 3. The distributions are centered on 0 km s^{-1} within statistical uncertainty. The double-Gaussian distribution (solid black line) was empirically derived. The velocity difference is defined in Equation (3) using the redshift difference in place of the absolute difference.

sample” of quasars in DR16Q. The full sample consists only of quasars where $0 < Z \leq 5.0$ and $0 < Z_{\text{PCA}} \leq 5.0$, and each source subsample was drawn from this greater set.

The full distribution of Δv for the samples in Table 4 can be seen in the left-hand panel of Figure 5. The right-hand panel shows Δv as a function of Z_{PCA} for catastrophic failures in the full sample. The lines appearing near 9900 km s^{-1} and $10,500 \text{ km s}^{-1}$ are artifacts of edge effects due to how the PCA-fitting algorithm bins redshift ranges.

Over the entire sample (marked “TOTAL” in Table 4) the catastrophic failure rate for the Z column is 0.93%. It should be noted that the PCA redshift, itself, is likely not an ideal estimate of a quasar’s host redshift. In addition, the PCA-fitting algorithm shares many properties with the SDSS pipeline ($\text{SOURCE_Z} = \text{“PIPE”}$), so Z_{PIPE} and Z_{PCA} might be expected to be similar.

5. Damped Lyman Alpha and Broad Absorption-line Systems

As was the case for previous SDSS quasar catalogs, DR16Q includes information about DLA systems (henceforth DLAs) and BAL quasars (henceforth BALs). For DR16Q, we used automated processes rather than visual inspections to identify DLAs and BALs, but BALs identified in previous visual

inspection campaigns still retain that classification independent of the processes described in this section.

5.1. Damped Lyman Alpha systems

We identified DLAs in DR16Q quasar spectra using the algorithm described in Parks et al. (2018), which is based on a convolutional neural network (CNN; see Parks et al. 2018 for full details).

We only classified DLAs in spectra with $2 \leq Z_{\text{PCA}} \leq 6$, the redshift range over which spectra contained enough pixels to reliably identify DLAs. We thus reduced the input set to 270,315 sight lines. If multiple observations were available for one object in the spAll-v5_13_0 file, we used the stacked spectrum of all good observations as input to the DLA finder. We identified bad spectra using the ZWARNING parameter (see, e.g., Section 3.2). If ZWARNING was SKY, LITTLE_COVERAGE, UNPLUGGED, BAD_TARGET, or NODATA, we did not use the associated observation in the stack. Following Parks et al. (2018), we provide a very pure sample that has a confidence parameter of more than 0.9, and logarithms of the column densities of more than 20.3. Our final sample contains 39,514 DLAs in 35,686 sight lines with an average logarithmic column density of 20.606. For each quasar spectrum, we provide the list of identified DLAs with the absorption redshifts (Z_{DLA}), the logarithms of the column density (NHI_{DLA}), and the confidence parameters (CONF_{DLA}). The size of each list is the same and corresponds to the maximum number of identified DLAs in any spectrum. If all parameters are set to -1 , then no DLA was detected. More information about the efficiency and purity of the aforementioned algorithm is forthcoming in S. Chabanier et al. (2020, in preparation).

5.2. Broad Absorption-line systems

We identified BALs in all quasars at $1.57 \leq z \leq 5.6$ using an algorithm that looks for absorption troughs that would represent either blueshifted C IV or Si IV features. We performed a χ^2 fit of an unabsorbed quasar model to each spectrum, looked for differences between the model and spectrum that would represent absorption, masked out these regions, and iterated these steps until no new absorption features are identified. This procedure is very similar to the method described by Guo & Martini (2019) to prepare DR14 quasar spectra for input to their CNN and used the same five principal components. We performed this fit over the rest-frame wavelength range 1260–2400 Å when possible, and a shorter range for the lowest- and highest-redshift quasars. If the χ^2 value of this fit was worse than the χ^2 value of the best pipeline

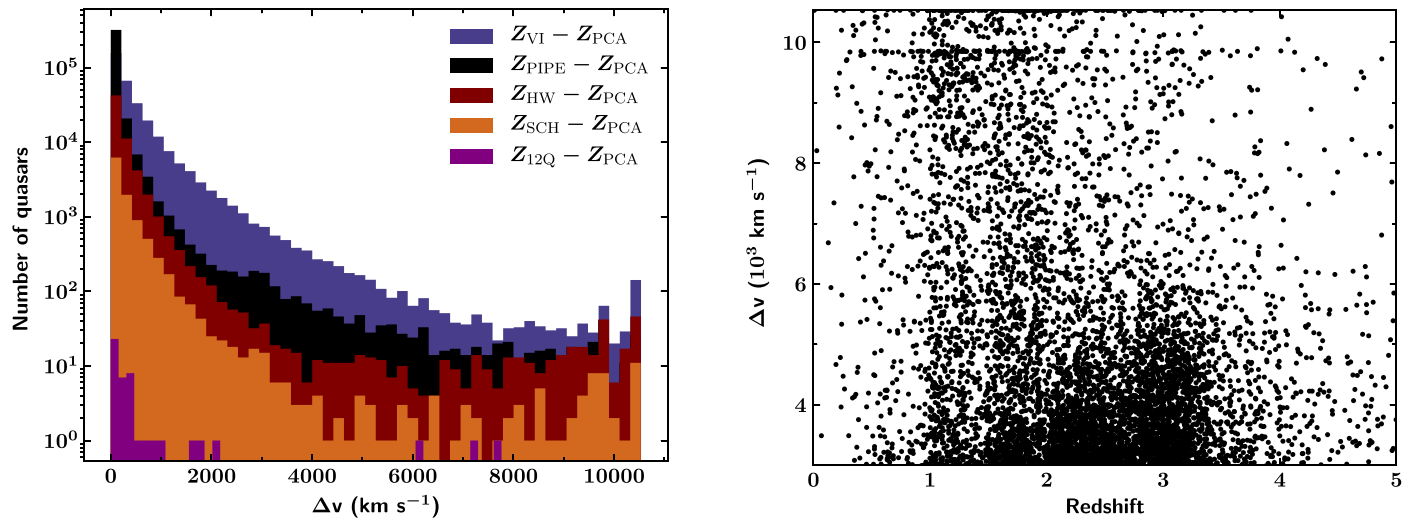


Figure 5. Left: the distribution of velocity differences between different redshift values and Z_{PCA} for quasars, where Δv is defined by Equation (3). The five distributions overlap; they are not vertically stacked. Right: the velocity difference as a function of the PCA redshift for catastrophic failures. A catastrophic failure is defined as $\Delta v > 3000 \text{ km s}^{-1}$. The horizontal lines that appear around 9900 and $10,500 \text{ km s}^{-1}$ are artifacts of edge effects due to the PCA-fitting algorithm binning method.

fit, we used that pipeline fit instead. We then normalized the spectrum by the best model.

The algorithm measured the commonly used “BALnicity index” (BI) proposed by Weymann et al. (1991) and the intrinsic absorption index (AI) proposed by Hall et al. (2002). BI was computed using

$$\text{BI} = - \int_{25000}^{3000} \left[1 - \frac{f(v)}{0.9} \right] C(v) dv, \quad (4)$$

where $C(v) = 0$, unless $1 - f(v)/0.9$ is continuously positive over a velocity interval $\Delta v \geq 2000 \text{ km s}^{-1}$, in which case $C(v) = 1$. $f(v)$ is the normalized flux density as a function of velocity blueshift from the C IV or Si IV emission-line center. AI was computed by

$$\text{AI} = - \int_{25000}^0 \left[1 - \frac{f(v)}{0.9} \right] C(v) dv, \quad (5)$$

where $C(v)$ and $f(v)$ have the same definition as Equation (4). DR16Q contains any BI and AI measurements for both C IV and Si IV for all quasars with $1.57 \leq z \leq 5.6$. These are BI_CIV, AI_CIV, BI_SIIIV, and AI_SIIIV. We also provide error estimates for each quantity: ERR_BI_CIV, ERR_AI_CIV, ERR_BI_SIIIV, and ERR_AI_SIIIV. All BI, AI, and error estimates are in units of km s^{-1} .

We assigned a BAL probability BAL_PROB to each quasar based on the statistical significance of the troughs associated with the C IV line and the quality of the χ^2 fit to the quasar continuum. The BAL_PROB values are one of four discrete values and are based on visual inspection of large numbers of quasars whose BI values and continuum fits have different levels of statistical significance. For quasars with good continuum fits, we assigned BAL_PROB = 1 to cases where BI_CIV is more than ten times the uncertainty in this quantity. Based on our visual inspections, these are all unambiguous cases. Quasars with a less significant BI measurement, but whose AI_CIV is more than 10 times the uncertainty, were assigned BAL_PROB = 0.95. These are nearly all unambiguous BALs as well. If BI_CIV is zero, but AI is similarly significant, we assigned BAL_PROB = 0.9. These are nearly all

BALs, but their BI value is zero where the trough is under 2000 km s^{-1} wide and/or the trough extends closer to the line center than 3000 km s^{-1} . Other quasars with a less significant BI measurement were assigned BAL_PROB = 0.75, and quasars with a BI_CIV value of zero and a less significant AI value were assigned BAL_PROB = 0.5. We used similar criteria to assign BAL_PROB to quasars with poorer continuum fits, although with generally lower probability values. For a small number of quasars, the continuum fit failed, and these quasars were not assigned a value for BAL_PROB. The remaining quasars were assigned BAL_PROB = 0.

6. Summary of Quasar Characteristics

DR16Q comprises two catalog files: a superset of objects targeted as quasars by SDSS-I/II/III/IV and a quasar-only set selected from that superset. The superset contains 1,440,615 observations and includes quasars from BOSS and eBOSS, legacy quasars added from DR7Q, and serendipitous discoveries added from DR12Q. The quasar-only catalog contains 750,414 quasars, where 225,082 are new quasars observed since DR14Q. Quasars appearing in DR16Q can be identified using the unique combination of plate, MJD, and fiber ID. The plate, MJD, and fiber ID of “duplicate observations” have also been back-populated into the superset for user convenience, though each observation still appears in its own record. We have also marked which quasars are considered primary in the PRIM_REC field, which only appears in the superset. Due to catalog construction constraints in DR7Q, there are possible additional duplicate observations from SDSS-I/II that are not included in DR16Q. DR16Q represents the largest catalog of quasars to date taken from SDSS data and covers 9376 deg^2 of the sky, with an average on-sky surface density of $\sim 80 \text{ deg}^{-2}$. DR16Q also presents the largest variety of redshift estimates, to date, for each quasar in an SDSS quasar catalog and is the first such catalog to include the Gaia DR2 data for known quasars.

The left-hand panel of Figure 6 presents the redshift distribution of the number of observed quasars for each SDSS campaign as they appear in the DR16Q quasar-only catalog. The number of observed quasars increased dramatically during

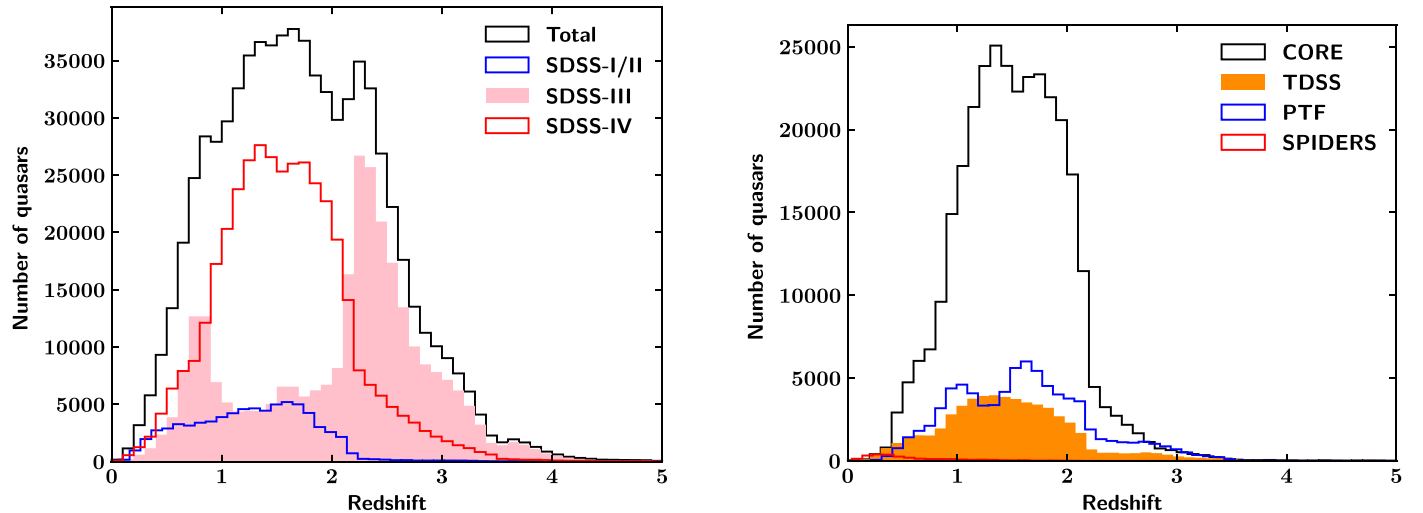


Figure 6. Left: the number of DR16Q quasars as a function of the PCA redshift, Z_{PCA} , for different SDSS spectroscopic campaigns. Right: the number of SDSS-IV/eBOSS quasars in DR16Q, separated by eBOSS subprogram. Both: only quasars where $0 < Z_{\text{PCA}} \leq 5$ were used.

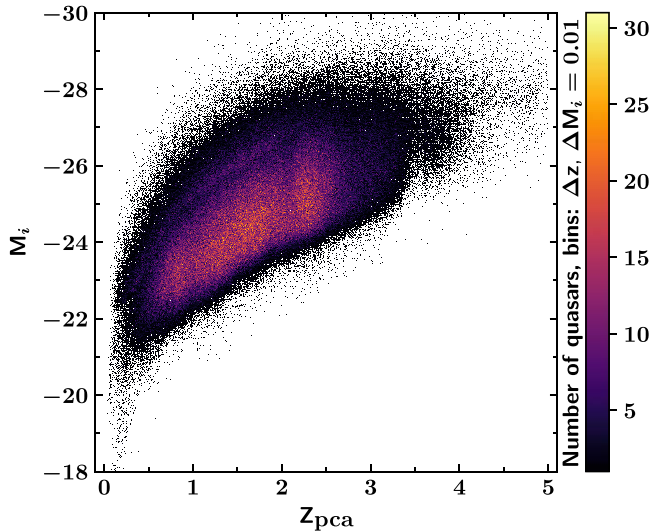


Figure 7. The distribution of absolute i -band magnitudes, $M_i[z=2]$, as a function of the PCA redshift, Z_{PCA} . Magnitudes and redshifts were separated into bins of size $\Delta Z_{\text{PCA}} = 0.01$ and $\Delta M_i = 0.01$. See Section 8 for details on how $M_i[z=2]$ was calculated. Only quasars that were detected at 1σ in the i band are included in the plot.

the SDSS-III/BOSS campaign, which targeted fainter quasars at higher redshift. The right-hand panel of Figure 6 shows the redshift distribution of only the SDSS-IV/eBOSS quasars broken down by the eBOSS subprogram. Quasars in each panel use the PCA-derived redshift for consistency and are limited to quasars where $0 < Z_{\text{PCA}} \leq 5$. It is clear that SDSS-IV contributes the most SDSS quasars and that by far the eBOSS CORE sample contributes the most SDSS-IV quasars. The luminosity space of the quasars in DR16Q is shown in Figure 7, as a function of the same PCA redshifts.

7. Multiwavelength Data

DR16Q includes force-photometered or cross-matched data from the Galaxy Evolution Explorer (GALEX; Martin et al. 2005), the UKIRT Infrared Deep Sky Survey (UKIDSS; Lawrence et al. 2007), the Wide-Field Infrared Survey Explorer (WISE; Wright et al. 2010), the FIRST radio survey

(Becker et al. 1995), the Two Micron All Sky Survey (2MASS; Skrutskie et al. 2006), the Second ROSAT All-Sky Survey (2RXS; Boller et al. 2016), the Third XMM-Newton Serendipitous Source Catalog (Rosen et al. 2016), and Gaia data release 2 (Gaia Collaboration et al. 2018). In this section, we describe how we incorporated these multiwavelength data into DR16Q. For GALEX, UKIDSS, and WISE, we cross-matched to the data releases that were actually used to target quasars in BOSS and eBOSS. These multiwavelength data, then, are particularly useful for trying to recreate BOSS/eBOSS targeting. As FIRST, 2MASS, ROSAT, XMM-Newton, and Gaia were not used in BOSS/eBOSS targeting, we chose to cross-match to the most recent data set available during catalog construction. The data set used for each external survey is explicitly defined in that survey’s subsection.

A summary of these external surveys can be found in Table 5, with more detailed information in the appropriate subsections below. In Figure 8 we demonstrate the utility of these data by providing the spectral energy distribution of a quasar that has extensive multiwavelength coverage in DR16Q.

7.1. GALEX

As in past SDSS quasar catalogs, DR16Q includes data from GALEX Data Release 5, force-photometered at the location of SDSS DR8 imaging sources (Aihara et al. 2011). We present data from both GALEX bands: NUV (1350–1750 Å) and FUV (1750–2750 Å). A total of 646,041 objects have a nonzero flux in either the NUV or FUV band, 552,025 (431,431) have a positive NUV (FUV) flux, and 386,642 objects have a positive flux in both bands. All fluxes are reported in nanomaggies,⁴⁰ where 1 nanomaggy $\approx 3.631 \times 10^{-6}$ Jy.

7.2. UKIDSS

Similarly to GALEX, DR16Q includes SDSS-DR8-based imaging force-photometered in the four UKIDSS bands (with central wavelengths): Y (1.02 μm), J (1.25 μm), H (1.63 μm), and K (2.20 μm) bands. UKIDSS data were taken before March 2011 and was released as UKIDSS DR1–DR9 (see Section

⁴⁰ See <https://www.sdss.org/dr16/algorithms/magnitudes/#Fluxunits:maggiesandnanomaggies>.

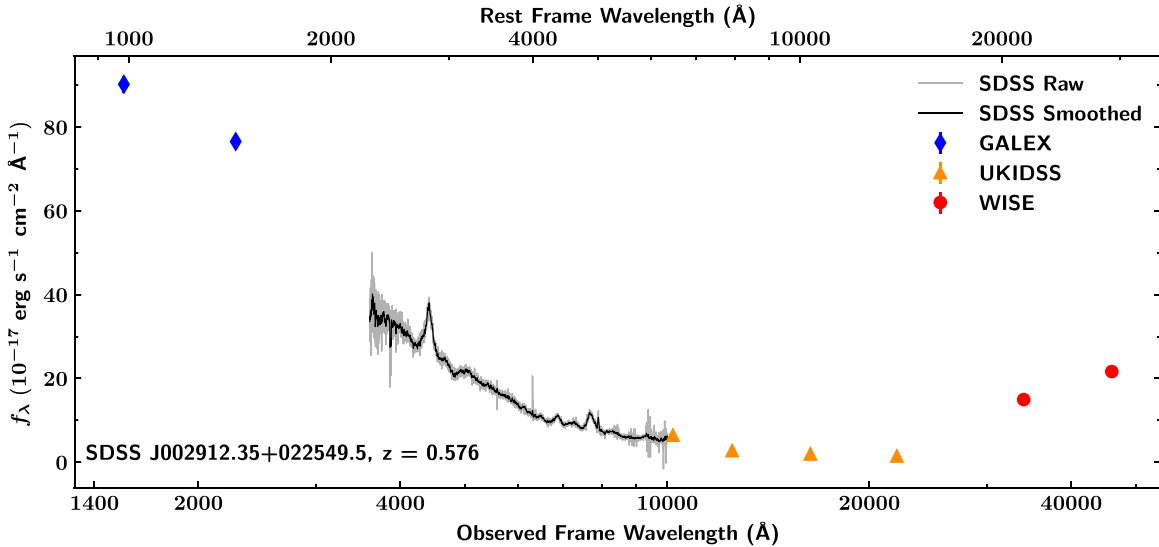


Figure 8. The spectral energy distribution for the quasar SDSS J002912.35+022549.5 (plate 7855, MJD 57011, fiber ID 530). Data are included from GALEX, SDSS, UKIDSS, and WISE. The SDSS spectrum (gray) has been smoothed (black) using a boxcar with a width of 8.4 Å (10 pixels). Error bars for GALEX, UKIDSS, and WISE data are included, but are too small to be visible at this scale. In the SDSS spectrum the Mg II $\lambda 2799$, H β , and H γ emission lines can be clearly distinguished. SDSS J002912.35+022549.5 also has data in DR16Q from FIRST, ROSAT/2RXS, and Gaia.

Table 5
Summary of Multiwavelength Surveys

Survey	Passband Centers	Number of DR16Q Sources
GALEX (Section 7.1)	UV (NUV, 1350–1750 Å; FUV (1750–2750 Å)	646,041
UKIDSS (Section 7.2)	Infrared (Y , 1.02 μm ; J , 1.25 μm ; H , 1.63 μm ; K , 2.20 μm)	151,362
WISE (Section 7.3)	Infrared ($W1$, 3.4 μm ; $W2$, 4.6 μm)	747,962
FIRST (Section 7.4)	Radio (20 cm)	21,843
2MASS (Section 7.5)	Infrared (J , 1.25 μm ; H , 1.65 μm ; K_s , 2.16 μm)	18,115
ROSAT/2RXS (Section 7.6)	X-ray (0.5–2.0 keV)	11,545
XMM-Newton (Section 7.7)	X-ray (Soft, 0.2–2.0 keV; Hard, 2.0–12.0 keV)	18,138
Gaia (Section 7.8)	Optical (G , 3300–10500 Å; BP , 3300–6800 Å; RP , 6300–10500 Å)	469,786

4.5.5 of Pâris et al. 2014). We provide the fluxes and errors for each of these bands in units of $\text{W m}^{-2} \text{Hz}^{-1}$.

DR16Q contains 151,362 measurements from the UKIDSS area (which is smaller than the SDSS footprint). [150,147, 149,629, 149,502, and 150,288] sources have a positive flux in [Y , J , H , and K] respectively. A total of 146,500 sources have a positive flux in all four bands.

7.3. WISE

eBOSS targeting was, in part, based on data taken from the WISE $W1$ (3.4 μm) and $W2$ (4.6 μm) bands (Myers et al. 2015). Many of the eBOSS quasar targets had fluxes below the WISE detection limit used for the AllWISE Data Release, so forced photometry was applied to custom “unWISE” stacks (Lang 2014), as described in Lang et al. (2016).⁴¹

DR16Q contains 747,962 objects with a positive flux in either the $W1$ or $W2$ bands. There are 744,835 (741,227) objects with a positive flux in the $W1$ ($W2$) band, and 739,093 objects with a positive flux in both bands. Quasars in DR16Q that were not identified using SDSS imaging do not have “unWISE” forced photometry. There are 1001 such objects in DR16Q, and each has a flux set to -1 in both bands.

⁴¹ For more information, see https://www.sdss.org/dr15/data_access/value-added-catalogs/?vac_id=wise-forced-photometry.

7.4. FIRST

Sources in DR16Q are matched to the 2014 December version of the FIRST⁴² catalog (e.g., Helfand et al. 2015), using a $2.^{\circ}0$ radius. Our reported FIRST_FLUX corresponds to the peak flux density, in mJy, at 20 cm wavelength. These values include the added 0.25 mJy “CLEAN” bias described in Thyagarajan et al. (2011). We also report the FIRST S/N of the peak flux using

$$\text{S/N} = \frac{f_{\text{peak}} - 0.25}{f_{\text{rms}}}. \quad (6)$$

The catalog contains 21,843 matches to FIRST radio sources.

7.5. 2MASS

DR16Q includes data from the 2MASS All-Sky Point Source Catalog, released March 2003, in three bands (with central wavelengths): J (1.25 μm), H (1.65 μm), and K_s (2.16 μm). Catalog objects were matched to 2MASS sources within $2.^{\circ}0$, and we include the Vega magnitude, magnitude uncertainty, S/N, and photometric read flag for each object. There are a total of 18,115 2MASS matches in DR16Q. The magnitude limits of the 2MASS survey ($J < 15.8$, $H < 15.1$,

⁴² <http://sundog.stsci.edu/first/catalogs.html>

and $K_s < 14.3$) explain the lower detection rate compared to WISE and UKIDSS.

7.6. ROSAT/2RXS

Unlike the other surveys mentioned in this section, a single coordinate-match with the ROSAT/2RXS (Boller et al. 2016) and XMMSL2⁴³ (Saxton et al. 2008) would not provide a reliable association. This is because both surveys have a large positional uncertainty, as can be seen in Figure 1 of Salvato et al. (2018). In particular, 95% of the 2RXS sources have a 1σ positional uncertainty smaller than $29''$. As detailed in Dwelly et al. (2017), Salvato et al. (2018), and Comparat et al. (2020), a better approach is to construct a match between X-ray sources and AllWISE sources via a Bayesian approach (using a code called `Nway`). Here, we simply matched the coordinates of DR16Q within $1''$ to the AllWISE counterparts of the X-ray sources presented in Salvato et al. (2018).

In DR16Q there are a total of 11,545 matched objects, and we include the 2RXS R.A. and decl., and the source flux and flux error in the 0.5–2.0 keV band.

7.7. XMM-Newton

DR16Q includes cross-matches to the two most complete X-ray catalogs to date: XMMPZCAT⁴⁴ (Ruiz et al. 2018) and 3XMM-DR8,⁴⁵ which are both based on the third version of the XMM-Newton Serendipitous Source Catalog (Rosen et al. 2016).

XMMPZCAT (Ruiz et al. 2018) is a catalog of photometric redshifts for X-ray sources, which was created using a machine-learning algorithm (MLZ-TPZ; detailed in Carrasco Kind & Brunner 2013). XMMPZCAT provides X-ray positions and redshifts for about 100,000 sources. We cross-matched DR16Q and XMMPZCAT, with a matching radius of $10''$. Despite the large matching radius, 59% of the sources were within $1''$. DR16Q includes more than 15,800 sources with X-ray counterparts in XMMPZCAT, of which $\sim 9\%$ are estimated to be contaminants due to chance superpositions.

XMMPZCAT is based on 3XMM-DR6 (the sixth release of the 3XMM catalog). So, in addition, we matched DR16Q to the more recent 3XMM-DR8 catalog using a $5.''0$ radius. We restricted this match to areas not covered by 3XMM-DR6 or to sources without XMMPZCAT counterparts. DR16Q contains an additional ~ 2300 X-ray counterparts from 3XMM-DR8.

For each of the 18,138 DR16Q quasars with XMM-Newton counterparts, we report the soft (0.2–2.0 keV), hard (4.5–12.0 keV), and total (0.2–12.0 keV) fluxes with associated errors. These were computed as the weighted average of all detections in the three XMM-Newton cameras (MOS1, MOS2, PN). The X-ray luminosities for the total fluxes were also computed and are provided. These are not absorption corrected. All fluxes and errors are expressed in $\text{erg s}^{-1} \text{cm}^{-2}$, and the total luminosity was computed using Z .

⁴³ For SL2 specifics, see <https://www.cosmos.esa.int/web/xmm-newton/xmmsl2-ug>.

⁴⁴ See http://xraygroup.astro.noa.gr/Webpage-prodex/xmmfitcat_access.html.

⁴⁵ See http://xmssc.irap.omp.eu/Catalogue/3XMM-DR8/3XMM_DR8.html.

7.8. Gaia

DR16Q includes data from the second data release of Gaia.⁴⁶ We matched objects using a $0.''5$ radius and present the Vega magnitudes and mean S/N for the three Gaia bands: G , BP , and RP , as well as the Gaia R.A., decl., parallax, and proper motion (for both R.A. and decl.). We also include the unique Gaia designation, which is guaranteed to remain unique in future Gaia data releases.

A total of 469,786 objects in DR16Q have a match to the Gaia catalog, to limiting magnitudes of $G < 22.0$, $BP < 23.6$, and $RP < 23.2$.

8. Description of the DR16Q Catalog

The DR16Q quasar-only catalog contains 183 columns of information for each quasar in a binary FITS (Wells et al. 1981) table file. The DR16Q superset includes the columns listed below up to column 98 inclusive, omitting `Z_LYAWG` and `M_I` (columns 53 and 97 respectively), but adding `PRIM_REC` (column 16 in the superset), which has a value of 1 if the record is considered the primary observation for a quasar. The columns in the quasar-only catalog are summarized in Table D1.

Complete DR16Q quasar-only column descriptions follow:

1. The SDSS name generated from the R.A. and decl. for the primary record in the format $hhmmss.ss \pm ddmmss.s$ in the J2000 equinox. The “SDSS J” is omitted. Coordinate values are truncated, not rounded.

2–3. The R.A. and decl. in decimal degrees for the J2000 equinox.

4–6. The unique spectroscopic plate number, modified Julian date of spectroscopic observation, and fiber ID. The combination of these three values gives a unique identifier for every spectroscopic observation in SDSS-I/II/III/IV. Where an object was observed multiple times we chose the observation with the most confident visual inspection. If data from visual inspection were not available, the observation with the highest `SN_MEDIAN_ALL` was chosen as the primary.

7. The automated classification as outlined in Section 3.2. This column can take the values `GALAXY`, `QSO`, `STAR`, `UNK`, and `VI`. A classification of `UNK` corresponds to objects that were added to the superset catalog after the initial automated classification was completed. All of these records were taken from a catalog of visually inspected objects that did not have a targeting bit that appears in Table 1.

8. The automated classification as detailed in the first part of Section 3.2. This column can take the same set of values as `AUTOCLASS_PQN`, and `UNK` is defined as above. Classifications of `STAR`, `GALAXY`, `QSO` were retained in `AUTOCLASS_PQN`. Only objects with a classification of `VI` in this column could be reclassified in `AUTOCLASS_PQN`.

9. A numeric flag indicating if an object was identified as a quasar by QuasarNET. A value of -1 indicates the object was not processed by QuasarNET, 1 (0) indicates the object was identified as a quasar (non-quasar).

10. The redshift of the quasar as computed by QuasarNET. As outlined in Section 3.2, this was used as a binary discriminant with a threshold set to $Z_{QN} = 2.0$. Observations with `AUTOCLASS_DR14Q` set to `VI` that had $Z_{QN} < 2.0$ were reclassified in `AUTOCLASS_PQN` as `QSO`.

⁴⁶ <https://www.cosmos.esa.int/web/gaia/dr2>

11. A binary flag indicating if the object was selected randomly for visual inspection as detailed in Section 3.4. A value of 0 indicates the object was not selected. The randomized subsample was selected from the superset and contained some duplicate observations of quasars. All subsampled 10,000 observations were unique. Objects were selected from a larger set where EBOSS_TARGET1 contained the QSO1_EBOSS_CORE targeting bit set or had an observation date ($MJD \geq 56839$) and pipeline redshift ≥ 1.8

12. The redshift from the visual inspection of the randomly selected subsample. Note that this field is included as a possible “visual inspection” source for Z .

13. The confidence rating for a visually identified redshift. A value of -1 indicates the object was not selected for the subsample. A value of 1 is the lowest confidence and 3 is the highest confidence. A value of 1 typically indicates a spectrum with only one broad emission peak above the noise spectrum.

14. A numeric flag indicating whether the automated pipeline correctly identified the classification and redshift with $\Delta v \leq 3000 \text{ km s}^{-1}$. A value of -1 indicates the record was not included in the random subsample, a value of 0 indicates the pipeline incorrectly identified the classification or redshift, and a value of 1 indicates that both classification and redshift were correct.

15. A numeric flag that classifies the record as a quasar for the randomly selected subsample. As in 13–14, a value of -1 indicates the record was not selected.

16. A 64 bit integer that identifies BOSS and eBOSS objects in the SDSS photometric and spectroscopic catalogs. Some SDSS-I/II objects have a THING_ID value, but not all. A value of -1 indicates the record was not assigned a THING_ID.

17. The visually identified redshift of the record. A value of -999 indicates a possible blazar, and no meaningful redshift from an emission feature can be identified. A value of -1 indicates the record was not visually inspected. See Section 4.3.

18. The confidence rating for the visually identified redshift. Objects with -1 were not visually inspected. Objects with 0 were visually inspected, but a confident redshift and classification could not be identified. For other objects, a value of 3 is the highest confidence.

19. The visually identified classification for the object. Definitions for the numeric values appear in Table 2. Objects appearing in DR16Q that have values of 1 (Star) or 4 (Galaxy) have low Z_{CONF} values. In these cases, the automated pipeline classification was used to determine whether the object was a quasar.

20–24. The redshift and flag indicating an object is a quasar for objects appearing in DR12Q (Pâris et al. 2017), DR7Q (Schneider et al. 2010), and Hewett & Wild (2010). These values are kept separate from Z_{VI} as an object observed more than once may have different redshifts for different pipeline reductions. For DR12Q objects, only the visual inspection redshift was recorded.

25. The Hewett & Wild (2010) redshifts applied to DR7Q and taken from the ancillary column of Shen et al. (2011). See column 143 at http://das.sdss.org/va/qso_properties_dr7/dr7.htm for more information.

26. The overall flag indicating if an object is a quasar. See Section 3.6.

27. The best available redshift taken from Z_{VI} , Z_{10K} , Z_{DR12Q} , $Z_{\text{DR7Q_SCH}}$, $Z_{\text{DR6Q_HW}}$, or Z_{PIPE} . Visually identified redshifts with $Z_{\text{CONF}} > 1$ were preferred.

$Z_{\text{DR6Q_HW}}$ was preferred over $Z_{\text{DR7Q_SCH}}$. In the absence of a confident visual inspection redshift or previous catalog redshift, this value is taken from Z_{PIPE} .

28. The source for the redshift recorded in column 27. DR12Q redshifts were taken from the visual inspection redshifts in that catalog.

29. The automated redshift taken from version v5_13_0 of the SDSS reduction pipeline. Objects added from DR7Q that had no BOSS or eBOSS reobservation do not have a pipeline redshift.

30. A bit flag for the quality of the pipeline redshift.⁴⁷

31. A string for the SDSS photometric identification generated from the sky version, run, rerun, camera column, field number, and ID. A blank value indicates the object does not have SDSS photometry and was selected as a target from another source catalog.

32–34. The redshift, warning flag, and $\Delta\chi^2$ for the PCA redshift generated by `redvsblue` (see Section 4.4).

35–52. Similar to columns 32–34, the `redvsblue` pipeline fits for six emission lines: H α , H β , Mg II, C III], C IV, and Ly α .

53. A PCA-derived redshift using `redvsblue` with spectrum-masking of the Ly α emission line and forest.

54–56. The absorber redshift, absorber column density, and confidence rating for DLA absorbers. No object had more than five absorbers. Objects with a value of -1 in the first element were either outside the redshift range for DLA systems or had no identifiable absorbers.

57. The probability an object is a BAL quasar. A -1 indicates the object’s redshift was too low to have a detection within the spectroscopic wavelength range.

58–65. The BALnicity index (BI), BI uncertainty, absorption index (AI), and AI uncertainty for the C IV region and for the Si IV region. All columns are in units of km s^{-1} .

66–71. Targeting bit flags for BOSS, eBOSS, and ancillary BOSS programs (see Table 1).

72–73. The number of additional spectra for an object from SDSS-I/II (column 72) or BOSS/eBOSS (column 73). Objects with only one observation will have both values set to 0. SDSS-I/II (SDSS-III/IV) objects have an MJD before (after) 54663.

74. The total number of additional spectroscopic observations for an object. This is the sum of columns 72 and 73. Objects with only one observation will have this value set to 0.

75–78. The spectroscopic plate, modified Julian date, fiber ID, and spectroscopic instrument for each duplicate observation of an object. As with columns 4–6, the combination of plate, MJD, and fiber ID provides a unique reference to each observation. For column 78, observations from SDSS-I/II have a value of 1, while observations from BOSS/eBOSS have a value of 2. Objects with multiple duplicate observations are in no particular order.

79–84. SDSS photometric information. Combining these columns gives the OBJID in column 31.

85. The wavelength for which the fiber placement was optimized to account for atmospheric differential refraction (Dawson et al. 2013), in angstroms.

86. The focal plane offset, in microns, to account for the wavelength dependence of the focal plane due to the distance from the center of the plate (Dawson et al. 2013).

87–88. The x and y positions in the focal plane for the spectroscopic fiber hole, in millimeters.

89–90. The name of the tiling chunk and the tile number for the spectroscopic plate placement on the sky.

⁴⁷ www.sdss.org/dr16/algorithms/bitmasks/#ZWARNING

91. The overall (S/N)² for the spectroscopic plate, taken from the minimum of the two red and two blue cameras for the plate.

92–93. The PSF flux and inverse variance for each of the five SDSS bands: *u*, *g*, *r*, *i*, and *z*, in nanomaggies. The fluxes are not corrected for Galactic extinction.

94–95. As for columns 92–93, but for inverse hyperbolic sine (asinh) AB magnitudes (Lupton et al. 1999). Magnitudes are not corrected for Galactic extinction.

96. The Galactic extinction values from Schlafly & Finkbeiner (2011) for the five SDSS bands.

97. Absolute *i*-band magnitude corrected for extinction. Calculated from the magnitude and Galactic extinction in columns 94 and 96, using the PCA redshift in column 32. *K* corrections were normalized to a redshift of 2, using Table 4 of Richards et al. (2006). The following cosmological parameters were used: $H_0 = 67.6 \text{ km s}^{-1} \text{ Mpc}^{-1}$, $\Omega_M = 0.31$, and $\Omega_\Lambda = 0.69$.

98. The median S/N for all good pixels in the five SDSS bands.

99. A matching flag for objects in the forced-photometry SDSS-DR8/GALEX catalog. A value of 1 (0) indicates the object was (was not) found in the GALEX catalog.

100–103. GALEX FUV and NUV fluxes and inverse variances, expressed in nanomaggies.

104. A matching flag for objects in the forced-photometry SDSS-DR8/UKIDSS catalog. A value of 1 (0) indicates the object was (was not) found in the UKIDSS catalog.

105–112. The flux density and error in the four UKIDSS bands (*Y*, *J*, *H*, and *K*) in units of $\text{W m}^{-2} \text{ Hz}^{-1}$.

113–114. The *W1*-band ($3.4 \mu\text{m}$) WISE flux and inverse flux variance in nanomaggies and nanomaggies^{−2}, respectively. A source with a measured magnitude of 22.5 in the Vega system would have a flux of 1 nanomaggy. See Lang et al. (2016).

115–116. The *W1*-band magnitude and magnitude uncertainty in the Vega magnitude system. Calculated using columns 113–114.

117. The *W1*-band profile-weighted χ^2 goodness of fit weighted by the point-spread function in the WISE images (for point sources).

118. The *W1*-band flux S/N. Calculated using columns 113–114.

119. The *W1*-band profile-weighted number of WISE exposures used in the “unWISE” coadd images for this source. This is analogous to a depth measurement.

120–121. The *W1*-band profile-weighted flux from other sources within the PSF of this source and the profile-weighted fraction of flux from external sources for this source.

122. The *W1*-band number of pixels included in the PSF fit for this source.

123–132. The *W2*-band ($4.6 \mu\text{m}$) data conforming to the descriptions in columns 113–122.

133. A matching flag for objects in the FIRST catalog. The maximum matching radius was $2.^{\circ}0$. A value of 1 (0) indicates the object did (did not) have a match in the FIRST catalog.

134–135. The peak flux density and flux density S/N at 20 cm in units of mJy. See Section 7.4.

136. The matching separation in arcseconds between the SDSS and FIRST objects.

137–138. The *J*-band magnitude and magnitude error from the 2MASS point source catalogs (Cutri et al. 2003). Objects used a maximum matching radius of $2.^{\circ}0$. Magnitudes are in the Vega system.

139–140. The *J*-band S/N and photometric read flag that records the default magnitude origins.⁴⁸

141–144. *H*-band data conforming to the descriptions in columns 137–140.

145–148. *K_s*-band data conforming to the descriptions in columns 137–140.

149. The matching separation in arcseconds between SDSS and 2MASS objects.

150. The 2RXS ID number designating unique objects.

151–152. The R.A. and decl. of the 2RXS source in decimal degrees (J2000).

153–154. The source flux and source flux error in the 0.5–2.0 keV band in $\text{erg s}^{-1} \text{ cm}^{-2}$, as described in Boller et al. (2016). $G = 2.4$ and dereddened.

155. The matching separation in arcsec between SDSS and 2RXS objects.

156. The XMM-Newton Source designation ID.

157–158. The R.A. and decl. of the XMM-Newton source in decimal degrees (J2000).

159–160. The X-ray flux and flux error for the 0.2–2.0 keV energy band in $\text{erg s}^{-1} \text{ cm}^{-2}$.

161–162. The X-ray flux and flux error for the 2.0–12.0 keV energy band in $\text{erg s}^{-1} \text{ cm}^{-2}$.

163–164. The total X-ray flux and flux error for the full energy range (0.2–12.0 keV) in $\text{erg s}^{-1} \text{ cm}^{-2}$.

165. The total X-ray luminosity for the full energy range (0.2–12.0 keV) in erg s^{-1} .

166. The matching separation in arcseconds between SDSS and XMM-Newton objects.

167. A matching flag for objects that appeared in the Gaia DR2 catalog. Objects were matched using a maximum radius of $0.^{\circ}5$. A value of 1 (0) indicates the object did (did not) have a match in the Gaia catalog.

168. The unique Gaia designation.

169–170. The Gaia DR2 barycentric R.A. and decl. in decimal degrees (J2015.5).

171–172. The Gaia absolute stellar parallax and parallax error (J2015.5).

173–174. The proper motion and standard error of proper motion for R.A. in mas yr^{−1} (J2015.5).

175–176. The proper motion and standard error for decl. in the same form as columns 173–174.

177–178. The mean magnitude and mean flux over standard deviation for the Gaia *G* band in the Vega magnitude system.

179–180. *BP*-band data conforming to the descriptions in columns 177–178.

181–182. *RP*-band data conforming to the descriptions in columns 177–178.

183. The matching separation in arcseconds between SDSS and Gaia DR2.

9. Conclusion

In this paper, we detail DR16Q, the final SDSS-IV/eBOSS quasar catalog. The catalog consists of two subcatalogs: the DR16Q superset containing 1,440,615 observations targeted as quasars, and the quasar-only set containing 750,414 quasars. The quasar-only catalog includes 225,082 new quasars observed after the release of DR14Q, a 42% increase in the catalog size. We estimate the quasar-only catalog to be 99.8% complete with 0.3%–1.3% contamination. We include

⁴⁸ See https://old.ipac.caltech.edu/2mass/releases/allsky/doc/sec2_2.html.

automated pipeline redshifts for all quasars observed as part of SDSS-III/IV and confident visual inspection redshifts for 320,161 quasars. DLAs and BALs were identified and measured by automated algorithms, and the quasar-only catalog includes 35,686 DLAs and 99,856 spectra with $BAL_PROB \geq 0.75$. DR16Q includes homogeneous redshifts derived using principal component analysis, including six separate emission-line PCA redshifts. Finally, DR16Q includes multiwavelength matching to GALEX, UKIDSS, WISE, FIRST, 2MASS, ROSAT/2RXS, XMM-Newton, and Gaia.

SDSS-IV/eBOSS observations are now complete, and SDSS-V (Kollmeier et al. 2017) will target far fewer quasars than SDSS-IV. DR16Q is therefore likely to remain the most significant compilation of SDSS quasars for quite some time to come.

B.W.L., J.N.M., and A.D.M. were supported by the US Department of Energy, Office of Science, Office of High Energy Physics, under award number DE-SC0019022. A.N.H. is supported by The University of Wyoming Science Initiative Wyoming Research Scholars Program and was funded by Wyoming NASA Space Grant Consortium, NASA grant #NNX15AI08H.

Funding for the Sloan Digital Sky Survey IV has been provided by the Alfred P. Sloan Foundation, the US Department of Energy Office of Science, and the Participating Institutions. SDSS-IV acknowledges support and resources from the Center for High-Performance Computing at the University of Utah. The SDSS website is www.sdss.org. In addition, this research relied on resources provided to the eBOSS Collaboration by the National Energy Research Scientific Computing Center (NERSC). NERSC is a U.S. Department of Energy Office of Science User Facility operated under contract No. DE-AC02-05CH11231.

SDSS-IV is managed by the Astrophysical Research Consortium for the Participating Institutions of the SDSS Collaboration including the Brazilian Participation Group, the Carnegie Institution for Science, Carnegie Mellon University, the Chilean Participation Group, the French Participation Group, Harvard-Smithsonian Center for Astrophysics, Instituto de Astrofísica de Canarias, The Johns Hopkins University, Kavli Institute for the Physics and Mathematics of the Universe (IPMU), University of Tokyo, the Korean Participation Group, Lawrence Berkeley National Laboratory, Leibniz Institut für Astrophysik Potsdam (AIP), Max-Planck-Institut für Astronomie (MPIA Heidelberg), Max-Planck-Institut für Astrophysik (MPA Garching), Max-Planck-Institut für Extraterrestrische Physik (MPE), National Astronomical Observatories of China, New Mexico State University, New York University, University of Notre Dame, Observatório Nacional, MCTI, The Ohio State University, Pennsylvania State University, Shanghai Astronomical Observatory, United Kingdom Participation Group, Universidad Nacional Autónoma de México, University of Arizona, University of Colorado Boulder, University of Oxford, University of Portsmouth, University of Utah, University of Virginia, University of Washington, University of Wisconsin, Vanderbilt University, and Yale University.

Appendix A Statistical Uncertainties in the Pipeline and PCA Redshifts

Figure A1 shows the distribution of the statistical uncertainty for Z_{pipe} and Z_{PCA} together with a redshift-dependent Gaussian distribution following the eBOSS requirements listed in

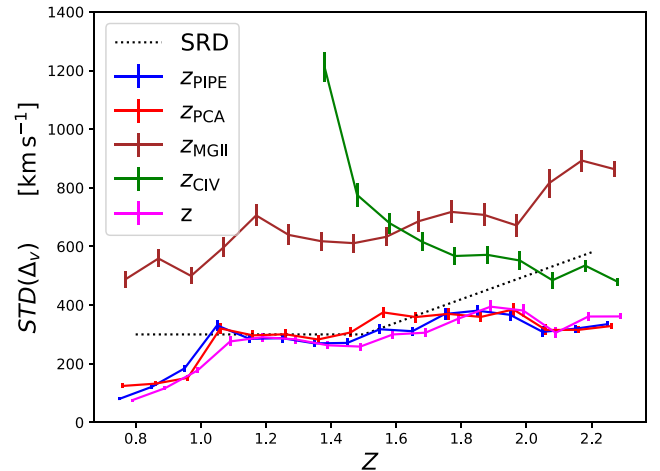


Figure A1. The distribution of statistical uncertainty for the redshift sources appearing in Figure 3 modeled with the redshift-dependent double-Gaussian profile defined in Equation (A1). Z (pink solid line) meets the requirement for statistical uncertainty defined in Dawson et al. (2016, black dotted line).

Dawson et al. (2016) for “low-” ($z < 1.5$) and “high-”redshift ($z > 1.5$) quasars.⁴⁹ As noted in Section 4.6, the actual distribution of redshift uncertainty contains tails extending to $|\Delta v| = 3000 \text{ km s}^{-1}$, which are not captured by a single-Gaussian model. Therefore, we considered a more realistic model based on a double-Gaussian profile (see the black curve in Figure 4) defined by

$$\frac{dN}{d(\delta\nu)} = \frac{1}{\sqrt{2\pi}(1+f)} \left[\frac{f}{\sigma_1} \exp \frac{-\Delta\nu^2}{2\sigma_1^2} \frac{1}{\sigma_2} \exp \frac{-\Delta\nu^2}{2\sigma_2^2} \right], \quad (\text{A1})$$

where both Gaussian functions are centered on zero. The resulting fit to the data gives $\sigma_1 = 150 \text{ km s}^{-1}$, $\sigma_2 = 1000 \text{ km s}^{-1}$, and $f = 4.478$. We kept the shape of this distribution fixed with redshift. A detailed study of the impact of this modeled, double-Gaussian redshift uncertainty on the cosmological parameters, using N -body mock catalogs, is presented in Smith et al. (2020). In addition, the clustering analyses presented in Hou et al. (2020) incorporated this redshift uncertainty when deriving cosmological parameters. Based on the Hou et al. and Smith et al. analyses, the total errors (statistical and systematic) of Z_{pipe} and Z_{PCA} meet the eBOSS requirements detailed in Dawson et al. (2016), provided that we model the shape of the redshift accuracy and precision using Equation (A1).

As detailed in Section 4.6, we found that the catastrophic failure rate for DR16Q quasar redshifts is of order 1%, meeting the requirements quoted in Dawson et al. (2016). In Smith et al. (2020), the effect of the catastrophic failures was implemented in N -body mock catalogs, and the impact of these on cosmological constraints is studied. They found that even a catastrophic failure rate of over 1% is sufficiently small that constraints on the cosmological parameters from eBOSS quasars are unaffected.

Appendix B Interesting Spectra

DR16Q includes a wide range of illustrative quasar spectra. We have chosen to include four such interesting, unusual, or informative spectra in this appendix. For all of the spectra

⁴⁹ Specifically, Section 3.2, requirement 1, of Dawson et al. (2016).

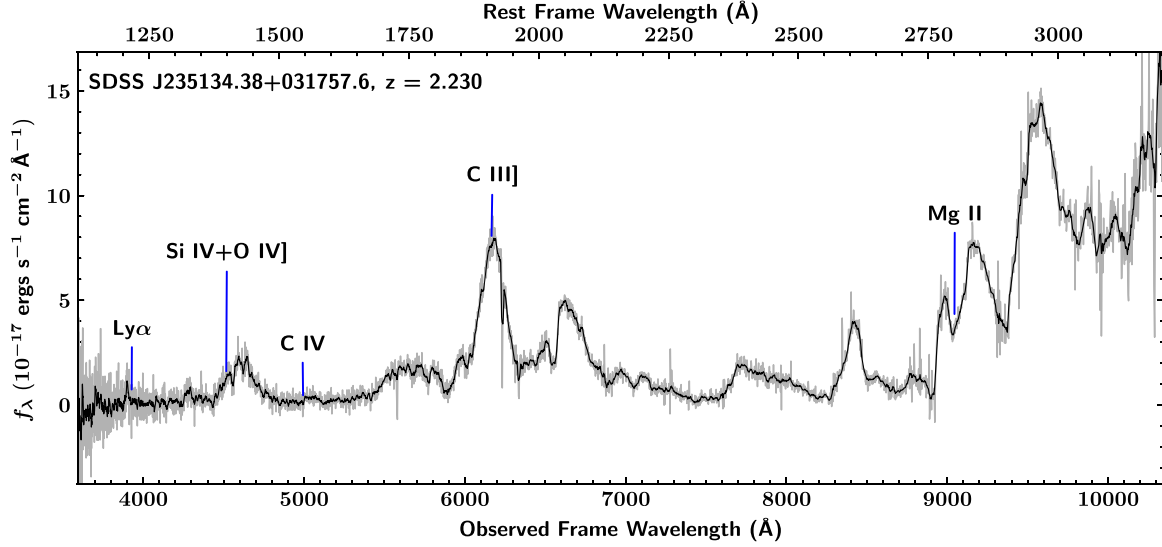


Figure B1. The FeLoBAL quasar SDSS J235134.38+031757.6, included in DR16Q under plate number 8741, MJD 57390, and fiber ID 450. Rest-frame wavelengths are plotted using the redshift $z = 2.230$ (obtained via a cross-correlation with similar FeLoBALs), although this spectrum was randomly selected for visual inspection (see Section 3.3) and assigned $z_{\text{VI}} = 2.43$. Locations of common quasar broad emission lines have been labeled (based on $z = 2.230$), though they do not obviously align with the broad features.

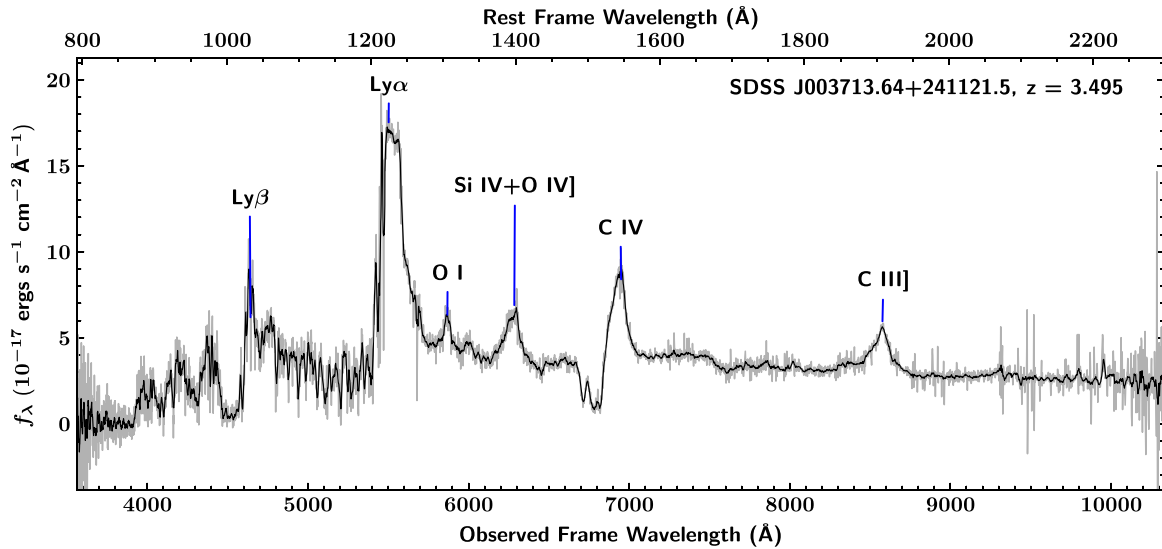


Figure B2. Quasar SDSS J003713.64+241121.5, included in DR16Q under plate number 7672, MJD 57339, and fiber ID 394, and with a redshift of $z_{\text{10K}} = 3.495$. This spectrum is an example of a BAL quasar. The Lyman limit can be clearly seen at 3900 \AA (observed frame). The spectrum also displays a typically weak O I $\lambda 1305$ broad emission line, which usually has flux relative to Ly α of $\sim 2\%$ (Vanden Berk et al. 2001). A (unlabeled) weak C II $\lambda 1336$ emission line can also be seen, which Vanden Berk et al. (2001) report having a flux relative to Ly α of $\sim 0.7\%$.

plotted here, the line rest wavelengths were taken from Table 2 of Vanden Berk et al. (2001).

In Figure B1, we present the spectrum of an iron low-ionization BAL (FeLoBAL) quasar discovered during the random visual inspections. For more information on these unusual objects, see Section 5.2 and Figure 6 of Hall et al. (2002).

DR16Q includes many BAL quasars. In Figure B2 we present a quasar that shows BAL features. These BAL features were identified by the algorithm described in Section 5.2. The spectrum also displays two emission lines that are often weak in quasars, O I $\lambda 1305$ (labeled) and C II $\lambda 1336$ (unlabeled).

The BAL algorithm described in Section 5.2 focuses on the C IV and Si IV features. In Figure B3, we present a different type: an Mg II BAL. This spectrum was not identified by the BAL algorithm as the quasar is not at a high-enough redshift for C IV or Si IV to be in the SDSS observable wavelength range.

SDSS-III/BOSS and SDSS-IV/eBOSS focused, in part, on studies of the Ly α forest using $z > 2.2$ quasars. In Figure B4, we include a spectrum of one such target that has a clearly visible Ly α forest. This spectrum highlights some rarer emission features and a weak Lyman limit.

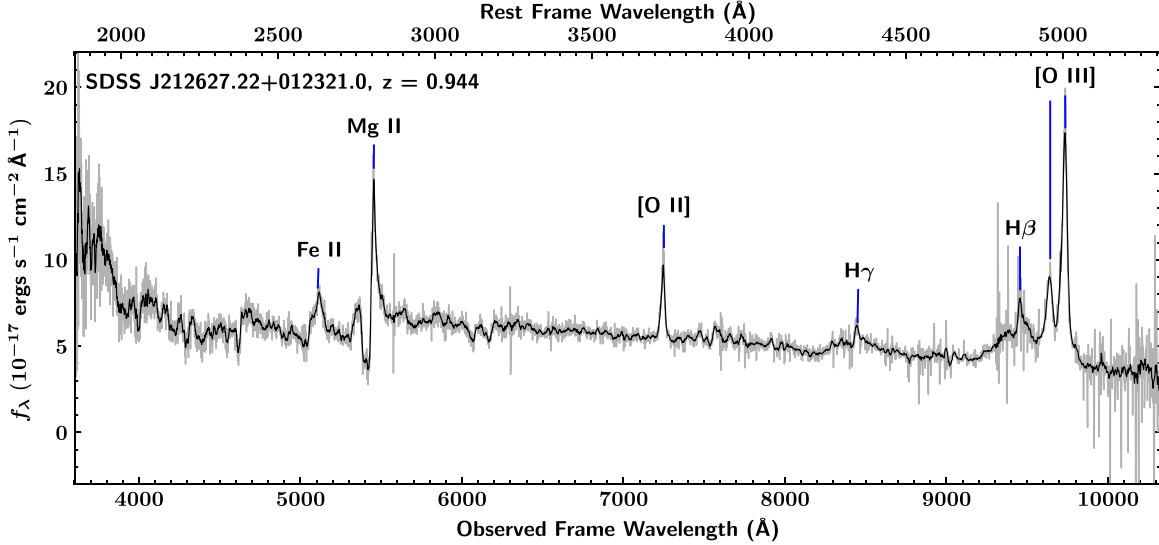


Figure B3. Quasar SDSS J212627.22+012321.0, included in DR16Q under plate number 9162, MJD 58040, fiber ID 354, and with a redshift of $z_{\text{10K}} = 0.944$. The spectrum shows a clear Mg II BAL feature along with a broad Fe II $\lambda 2627$ emission line.

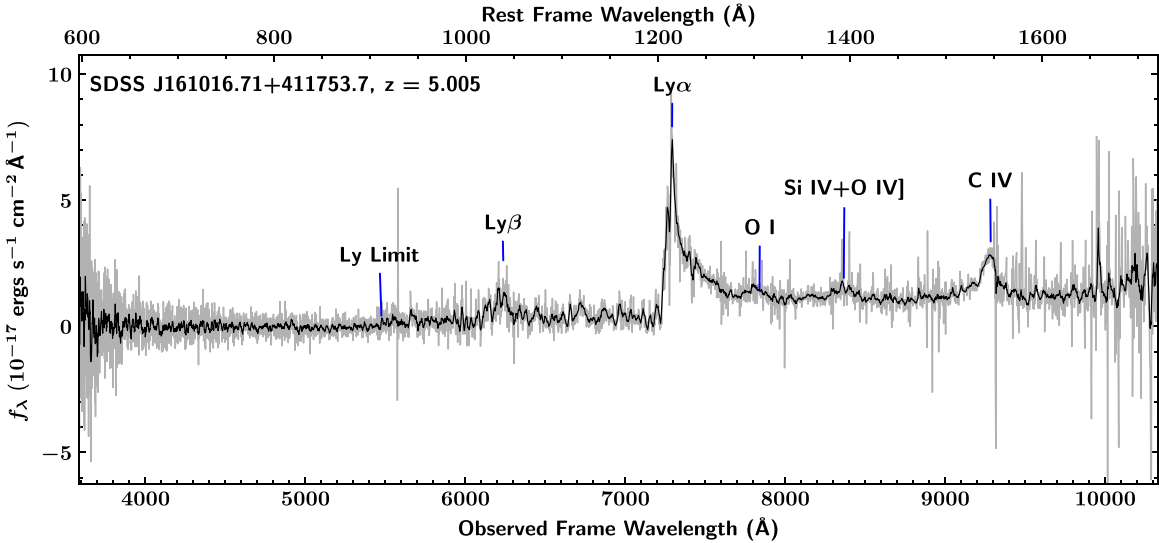


Figure B4. Quasar SDSS J161016.71+411753.7, included in DR16Q under plate number 6044, MJD 56090, fiber ID 418, and with a redshift of $z_{\text{VI}} = 5.005$. This higher-redshift spectrum is included as an example of a strong Ly α emission line with a visible, but weak, Ly α forest. The (weak) Lyman limit feature is labeled to show the edge of the forest region. The same O I $\lambda 1305$ feature seen in Figure B2 can be seen in this spectrum, though at a significantly reduced strength.

Appendix C Issues from Previous Quasar Catalogs

As large-scale usage of the SDSS quasar catalogs has increased over time, bugs have been discovered within previous iterations of these catalogs. Documented bugs and other issues that appeared in the 12th and 14th catalogs have been corrected for this iteration of the quasar-only and superset catalogs. We list the known issues below. All issues listed have been corrected in the most recent version of the catalogs released: DR16Q_v4 and DR16Q_Superset_v3 with one exception explained below.

1. (DR12Q) Incorrect astrometry for DR12Q objects.

- (a) DR12Q-added objects now use the current astrometric coordinates for BOSS objects.
- 2. (DR12Q) Absolute i -band magnitudes were incorrectly calculated. K corrections were only done to the continuum and did not include emission line corrections. Additionally, it appears the set cosmology parameters used were not either of the two sets published in the paper.
 - (a) K correction values were correctly applied and cosmology parameters match those listed in DR16Q.
- 3. (DR12Q, DR14Q) Spectra with ZWARNING flags for UNPLUGGED or BAD_TARGET were included.
 - (a) All records with these ZWARNING flags have been removed.

4. (DR14Q) Opening DR14Q reports a “VOTable opening error.”
 (a) VOTable errors have been corrected, and the first table HDU in the FITS files has been named “CATALOG.”
5. (DR14Q) DUPLICATE fields are populated with errant -1 values at every other position.
 (a) DUPLICATE fields have been populated with the correct PLATE, MJD, FIBERID, and SPECTRO values.
6. (DR14Q) SDSS names incorrectly reported due to erroneous rounding errors.
 (a) SDSS names are now correctly truncated, rather than rounded.
7. (DR14Q) OBJ_ID fields are blank.
 (a) The column has been renamed to OBJID to match other SDSS catalogs, and has been populated for BOSS and eBOSS objects. OBJID values for SDSS-I/II quasars have been included where they were available.
8. (DR14Q) GALEX_MATCHED and UKIDSS_MATCHED are recorded as floating numbers instead of integers.
 (a) These two fields are now recorded as integers and use 0 or 1 values to denote no-match or a match, respectively.
9. (DR14Q) FIRST_MATCHED uses incorrect values.
 (a) The FIRST_MATCHED column now uses 0 or 1 to denote a match.
10. (DR14Q) Records with no XMM or 2MASS match are blank.
 (a) Quasars with no match in XMM or 2MASS now have -1 values rather than blank entries.
11. (DR14Q) The following columns all had zero values or were empty: RUN_NUMBER, COL_NUMBER, RERUN_NUMBER, FIELD_NUMBER, SPECTRO_DUPLICATE.
 (a) These columns have been correctly populated.
12. (DR14Q) N_SPEC values did not match the number of additional spectra due to incorrect population of -1 values in the DUPLICATE fields (see #5 above).
 (a) The NSPEC fields have been populated correctly and renamed.
13. (DR14Q) Hyphens and periods appear in some column names. These may cause FITS reader programs to report errors.
 (a) All column names with hyphens or periods have been renamed to remove these punctuation marks. All columns now only use alphanumeric characters and underscores.
14. (DR14Q) Some TUNITS FITS header cards do not match the reported units.
 (a) All TUNITS header cards have been removed. Refer to this paper or the data model⁵⁰ for the correct units.
15. (DR14Q) The Z_ERR column did not contain errors for pipeline redshifts as reported.
 (a) The Z_ERR column has been removed.
16. (DR14Q) The ZWARNING column was not populated.
 (a) The ZWARNING column has been correctly populated for BOSS and eBOSS quasars.
17. (DR16Q) Six known quasars from DR7Q were not added to DR16Q and could not be included without affecting other SDSS projects in progress. These quasars can be found in the Science Archive Server (SAS) under the following PLATE-MJD-FIBERID combinations: 901-52641-307, 1194-52703-58, 1611-53147-507, 1768-53442-57, 1948-53388-42, and 2784-54529-73.

Appendix D FITS Table Description

The column descriptions (data model) for the DR16Q quasar-only catalog are summarized in Table D1. More detailed descriptions of each column can be found in Section 8.

Table D1
Format of the FITS Binary Table Containing DR16Q

Column	Name	Format	Description
1	SDSS_NAME	STRING	SDSS DR16 designation—hh:mm:ss.ss \pm dd:mm:ss.s (J2000)
2	RA	DOUBLE	Right ascension in decimal degrees (J2000)
3	DEC	DOUBLE	Declination in decimal degrees (J2000)
4	PLATE	INT32	Spectroscopic plate number
5	MJD	INT32	Modified Julian day of the spectroscopic observation
6	FIBERID	INT16	Spectroscopic fiber number
7	AUTOCLASS_PQN	STRING	Object classification post-QuasarNET
8	AUTOCLASS_DR14Q	STRING	Object classification based only on the DR14Q algorithm
9	IS_QSO_QN	INT16	Binary flag for QuasarNET quasar identification
10	Z_QN	DOUBLE	Redshift derived by QuasarNET
11	RANDOM_SELECT	INT16	Binary flag indicating objects selected for random visual inspection
12	Z_10K	DOUBLE	Redshift from visual inspection of random set
13	Z_CONF_10K	INT16	Confidence rating for visual inspection redshift of random set
14	PIPE_CORR_10K	INT16	Binary flag indicating if the automated pipeline classification and redshift were correct in the random set
15	IS_QSO_10K	INT16	Binary flag for random set quasar identification
16	THING_ID	INT64	SDSS identifier
17	Z_VI	DOUBLE	Redshift from visual inspection
18	Z_CONF	INT16	Confidence rating for visual inspection redshift
19	CLASS_PERSON	INT32	Object classification from visual inspection

⁵⁰ https://data.sdss.org/datamodel/files/BOSS_QSO/DR16Q/

Table D1
(Continued)

Column	Name	Format	Description
20	Z_DR12Q	DOUBLE	Redshift taken from DR12Q visual inspection
21	IS_QSO_DR12Q	INT16	Flag indicating if an object was a quasar in DR12Q
22	Z_DR7Q_SCH	DOUBLE	Redshift taken from DR7Q Schneider et al. (2010) catalog
23	IS_QSO_DR7Q	INT16	Flag indicating if an object was a quasar in DR7Q
24	Z_DR6Q_HW	DOUBLE	Redshift taken from DR6 Hewett & Wild (2010) catalog
25	Z_DR7Q_HW	DOUBLE	Redshift taken from the Shen et al. (2011) catalog ancillary columns. (See column 143 at http://das.dsoss.org/va/qso_properties_dr7/dr7.htm)
26	IS_QSO_FINAL	INT16	Flag indicating quasars included in final catalog
27	Z	DOUBLE	Best available redshift taken from Z_VI, Z_PIPE, Z_DR12Q, Z_DR7Q_SCH, or Z_DR6Q_HW
28	SOURCE_Z	STRING	Source for redshift in previous column
29	Z_PIPE	DOUBLE	Redshift from SDSS pipeline
30	ZWARNING	INT32	Quality flag on SDSS pipeline redshift estimate
31	OBJID	STRING	SDSS object identification number
32	Z_PCA	DOUBLE	PCA redshift derived by the <code>redvsblue</code> algorithm
33	ZWARN_PCA	INT64	Warning flag for <code>redvsblue</code> redshift
34	DELTACHI2_PCA	DOUBLE	$\Delta\chi^2$ for PCA redshift versus cubic continuum fit
35	Z_HALPHA	DOUBLE	PCA line redshift for H α from <code>redvsblue</code>
36	ZWARN_HALPHA	INT64	Warning flag for H α
37	DELTACHI2_HALPHA	DOUBLE	$\Delta\chi^2$ for H α line redshift versus cubic continuum fit
38	Z_HBETA	DOUBLE	PCA line redshift for H β from <code>redvsblue</code>
39	ZWARN_HBETA	INT64	Warning flag for H β
40	DELTACHI2_HBETA	DOUBLE	$\Delta\chi^2$ for H β line redshift versus cubic continuum fit
41	Z_MGII	DOUBLE	PCA line redshift for Mg II from <code>redvsblue</code>
42	ZWARN_MGII	INT64	Warning flag for Mg II
43	DELTACHI2_MGII	DOUBLE	$\Delta\chi^2$ for Mg II line redshift versus cubic continuum fit
44	Z_CIII	DOUBLE	PCA line redshift for C III] from <code>redvsblue</code>
45	ZWARN_CIII	INT64	Warning flag for C III]
46	DELTACHI2_CIII	DOUBLE	$\Delta\chi^2$ for C III] line redshift versus cubic continuum fit
47	Z_CIV	DOUBLE	PCA line redshift for C IV from <code>redvsblue</code>
48	ZWARN_CIV	INT64	Warning flag for C IV
49	DELTACHI2_CIV	DOUBLE	$\Delta\chi^2$ for C IV line redshift versus cubic continuum fit
50	Z_LYA	DOUBLE	PCA line redshift for Ly α from <code>redvsblue</code>
51	ZWARN_LYA	INT64	Warning flag for Ly α
52	DELTACHI2_LYA	DOUBLE	$\Delta\chi^2$ for Ly α line redshift versus cubic continuum fit
53	Z_LYAWG	FLOAT	PCA redshift derived from spectra masked blueward of Ly α .
54	Z_DLA	DOUBLE[5]	Redshift for damped Ly α features
55	NHI_DLA	DOUBLE[5]	Absorber column density for damped Ly α features
56	CONF_DLA	DOUBLE[5]	Confidence of detection for damped Ly α features
57	BAL_PROB	FLOAT	BAL probability
58	BI_CIV	DOUBLE	BALnicity index for the C IV region in km s $^{-1}$
59	ERR_BI_CIV	DOUBLE	Uncertainty of BI for the C IV region in km s $^{-1}$
60	AI_CIV	DOUBLE	Absorption index for the C IV region in km s $^{-1}$
61	ERR_AI_CIV	DOUBLE	Uncertainty of the absorption index for the C IV region in km s $^{-1}$
62	BI_SIIIV	DOUBLE	BALnicity index for the Si IV region in km s $^{-1}$
63	ERR_BI_SIIIV	DOUBLE	Uncertainty of BI for the Si IV region in km s $^{-1}$
64	AI_SIIIV	DOUBLE	Absorption index for the Si IV region in km s $^{-1}$
65	ERR_AI_SIIIV	DOUBLE	Uncertainty of the absorption index for the Si IV region in km s $^{-1}$
66	BOSS_TARGET1	INT64	BOSS target selection flag for the main survey
67	EBOSS_TARGET0	INT64	eBOSS target selection flag for the pilot survey (SEQUELS)
68	EBOSS_TARGET1	INT64	eBOSS target selection flag for the main survey
69	EBOSS_TARGET2	INT64	eBOSS target selection flag for the main survey
70	ANCILLARY_TARGET1	INT64	BOSS target selection flag for the ancillary surveys
71	ANCILLARY_TARGET2	INT64	BOSS target selection flag for the ancillary surveys
72	NSPEC_SDSS	INT32	Number of additional spectra from SDSS-I/II
73	NSPEC_BOSS	INT32	Number of additional spectra from BOSS/eBOSS
74	NSPEC	INT32	Total number of additional spectra
75	PLATE_DUPLICATE	INT32[74]	Spectroscopic plate number for duplicate spectrum
76	MJD_DUPLICATE	INT32[74]	Spectroscopic MJD for duplicate spectrum
77	FIBERID_DUPLICATE	INT16[74]	Spectroscopic fiber number for duplicate spectrum
78	SPECTRO_DUPLICATE	INT32[74]	Spectroscopic epoch for each duplicate, 1 = SDSS, 2 = (e)BOSS

Table D1
(Continued)

Column	Name	Format	Description
79	SKYVERSION	INT8	SDSS photometric sky version number
80	RUN_NUMBER	INT32	SDSS imaging run number of photometric measurements
81	RERUN_NUMBER	STRING	SDSS photometric processing rerun number
82	CAMCOL_NUMBER	INT32	SDSS camera column number (1–6)
83	FIELD_NUMBER	INT32	SDSS field number
84	ID_NUMBER	INT32	SDSS photometric ID number
85	LAMBDA_EFF	DOUBLE	Wavelength to optimize hold location for, in angstroms
86	ZOFFSET	DOUBLE	Backstopping offset distance in microns
87	XFOCAL	DOUBLE	Hole x-axis position in focal plane in millimeters
88	YFOCAL	DOUBLE	Hole y-axis position in focal plane in millimeters
89	CHUNK	STRING	Name of tiling chunk (from the plate-list product)
90	TILE	INT32	Tile number
91	PLATESN2	DOUBLE	Overall (S/N) ² measure for plate, minimum of all four cameras
92	PSFFLUX	FLOAT[5]	Flux in the <i>u</i> , <i>g</i> , <i>r</i> , <i>i</i> , <i>z</i> bands
93	PSFFLUX_IVAR	FLOAT[5]	Inverse variance of the <i>u</i> , <i>g</i> , <i>r</i> , <i>i</i> , <i>z</i> fluxes
94	PSFMAG	FLOAT[5]	PSF magnitudes in the <i>u</i> , <i>g</i> , <i>r</i> , <i>i</i> , <i>z</i> bands
95	PSFMAGERR	FLOAT[5]	Error on PSF magnitudes in the <i>u</i> , <i>g</i> , <i>r</i> , <i>i</i> , <i>z</i> bands
96	EXTINCTION	FLOAT[5]	Galactic extinction in the five SDSS bands (Schlafly & Finkbeiner 2011)
97	M_I	FLOAT	Absolute <i>i</i> -band magnitude, $M_i[z = 2]$ using Z_{PCA} redshift in Col. 32 See Section 8 for details on how $M_i[z = 2]$ was calculated.
98	SN_MEDIAN_ALL	DOUBLE	S/N median value for all good spectroscopic pixels
99	GALEX_MATCHED	INT16	GALEX matching flag
100	FUV	DOUBLE	<i>fuv</i> flux for GALEX
101	FUV_IVAR	DOUBLE	Inverse variance of the <i>fuv</i> flux
102	NUV	DOUBLE	<i>nuv</i> flux for GALEX
103	NUV_IVAR	DOUBLE	Inverse variance of the <i>nuv</i> flux
104	UKIDSS_MATCHED	INT16	UKIDSS matching flag
105	YFLUX	DOUBLE	<i>Y</i> -band flux density from UKIDSS (in $\text{W m}^{-2} \text{Hz}^{-1}$)
106	YFLUX_ERR	DOUBLE	Error in the <i>Y</i> -band flux density from UKIDSS (in $\text{W m}^{-2} \text{Hz}^{-1}$)
107	JFLUX	DOUBLE	<i>J</i> -band flux density from UKIDSS (in $\text{W m}^{-2} \text{Hz}^{-1}$)
108	JFLUX_ERR	DOUBLE	Error in the <i>J</i> -band flux density from UKIDSS (in $\text{W m}^{-2} \text{Hz}^{-1}$)
109	HFLUX	DOUBLE	<i>H</i> -band flux density from UKIDSS (in $\text{W m}^{-2} \text{Hz}^{-1}$)
110	HFLUX_ERR	DOUBLE	Error in the <i>H</i> -band flux density from UKIDSS (in $\text{W m}^{-2} \text{Hz}^{-1}$)
111	KFLUX	DOUBLE	<i>K</i> -band flux density from UKIDSS (in $\text{W m}^{-2} \text{Hz}^{-1}$)
112	KFLUX_ERR	DOUBLE	Error in the <i>K</i> -band flux density from UKIDSS (in $\text{W m}^{-2} \text{Hz}^{-1}$)
113	W1_FLUX	FLOAT	WISE flux in the <i>W1</i> band ($3.4 \mu\text{m}$; Vega, nanomaggies)
114	W1_FLUX_IVAR	FLOAT	Inverse variance of the <i>W1</i> -band flux (Vega, nanomaggies ⁻²)
115	W1_MAG	FLOAT	<i>W1</i> -band magnitude (Vega)
116	W1_MAG_ERR	FLOAT	<i>W1</i> -band uncertainty in magnitude (Vega)
117	W1_CHI2	FLOAT	Profile-weighted χ^2 for the <i>W1</i> band
118	W1_FLUX_SNR	FLOAT	Signal-to-noise ratio for the <i>W1</i> band from the flux and inverse variance
119	W1_SRC_FRAC	FLOAT	Fraction of source in profile-weighted fit
120	W1_EXT_FLUX	FLOAT	Amount of flux added to the profile by nearby sources
121	W1_EXT_FRAC	FLOAT	Fraction of profile flux from nearby sources
122	W1_NPIX	INT16	Number of pixels included in the profile fit
123	W2_FLUX	FLOAT	WISE flux in the <i>W2</i> band ($4.6 \mu\text{m}$) (Vega, nanomaggies)
124	W2_FLUX_IVAR	FLOAT	Inverse variance of the <i>W2</i> -band flux (Vega, nanomaggies ⁻²)
125	W2_MAG	FLOAT	<i>W2</i> -band magnitude (Vega)
126	W2_MAG_ERR	FLOAT	<i>W2</i> -band uncertainty in magnitude (Vega)
127	W2_CHI2	FLOAT	Profile-weighted χ^2 for the <i>W2</i> band
128	W2_FLUX_SNR	FLOAT	Signal-to-noise ratio for the <i>W2</i> band from flux and inverse variance
129	W2_SRC_FRAC	FLOAT	Fraction of source in the profile-weighted fit
130	W2_EXT_FLUX	FLOAT	Amount of flux added to the profile by nearby sources
131	W2_EXT_FRAC	FLOAT	Fraction of profile flux from nearby sources
132	W2_NPIX	INT16	Number of pixels included in the profile fit
133	FIRST_MATCHED	INT16	Matching flag for FIRST
134	FIRST_FLUX	DOUBLE	FIRST peak flux density at 20 cm in mJy
135	FIRST_SNR	DOUBLE	FIRST flux density S/N
136	SDSS2FIRST_SEP	DOUBLE	SDSS-FIRST separation in arcsec

Table D1
(Continued)

Column	Name	Format	Description
137	JMAG	DOUBLE	2MASS <i>J</i> -band magnitude (Vega)
138	JMAG_ERR	DOUBLE	2MASS error in the <i>J</i> -band magnitude
139	JSNR	DOUBLE	2MASS <i>J</i> -band S/N
140	JRDFLAG	INT32	2MASS <i>J</i> -band photometry flag
141	HMAG	DOUBLE	2MASS <i>H</i> -band magnitude (Vega)
142	HMAG_ERR	DOUBLE	2MASS error in the <i>H</i> -band magnitude
143	HSNR	DOUBLE	2MASS <i>H</i> -band S/N
144	HRDFLAG	INT32	2MASS <i>H</i> -band photometry flag
145	KMAG	DOUBLE	2MASS <i>K_s</i> -band magnitude (Vega)
146	KMAG_ERR	DOUBLE	2MASS error in the <i>K_s</i> -band magnitude
147	KSNR	DOUBLE	2MASS <i>K_s</i> -band S/N
148	KRDFLAG	INT32	2MASS <i>K_s</i> -band photometry flag
149	SDSS2MASS_SEP	DOUBLE	SDSS-2MASS separation in arcseconds
150	2RXS_ID	STRING	ROSAT ID
151	2RXS_RA	DOUBLE	Right ascension of the ROSAT source in decimal degrees (J2000)
152	2RXS_DEC	DOUBLE	Declination of the ROSAT source in decimal degrees (J2000)
153	2RXS_SRC_FLUX	FLOAT	ROSAT source flux in the 0.5–2.0 keV band in erg s ⁻¹ cm ⁻²
154	2RXS_SRC_FLUX_ERR	FLOAT	ROSAT source flux error in the 0.5–2.0 keV band in erg s ⁻¹ cm ⁻²
155	SDSS2ROSAT_SEP	DOUBLE	SDSS-ROSAT separation in arcseconds
156	XMM_SRC_ID	INT64	XMM source ID
157	XMM_RA	DOUBLE	Right ascension for XMM source in decimal degrees (J2000)
158	XMM_DEC	DOUBLE	Declination for XMM source in decimal degrees (J2000)
159	XMM_SOFT_FLUX	FLOAT	Soft (0.2–2.0 keV) X-ray flux in erg s ⁻¹ cm ⁻²
160	XMM_SOFT_FLUX_ERR	FLOAT	Error on the soft X-ray flux in erg s ⁻¹ cm ⁻²
161	XMM_HARD_FLUX	FLOAT	Hard (2.0–12.0 keV) X-ray flux in erg s ⁻¹ cm ⁻²
162	XMM_HARD_FLUX_ERR	FLOAT	Error on the hard X-ray flux from in erg s ⁻¹ cm ⁻²
163	XMM_TOTAL_FLUX	FLOAT	Total (0.2–12.0 keV) X-ray flux in erg s ⁻¹ cm ⁻²
164	XMM_TOTAL_FLUX_ERR	FLOAT	Error on the total X-ray flux in erg s ⁻¹ cm ⁻²
165	XMM_TOTAL_LUM	FLOAT	Total (0.2–12.0 keV) X-ray luminosity in erg s ⁻¹
166	SDSS2XMM_SEP	DOUBLE	SDSS-XMM-Newton separation in arcseconds
167	GAIA_MATCHED	INT16	Gaia matching flag
168	GAIA_DESIGNATION	STRING	Gaia designation, includes data release and source ID in that release
169	GAIA_RA	DOUBLE	Gaia barycentric right ascension in decimal degrees (J2015.5)
170	GAIA_DEC	DOUBLE	Gaia barycentric right declination in decimal degrees (J2015.5)
171	GAIA_PARALLAX	DOUBLE	Absolute stellar parallax (J2015.5)
172	GAIA_PARALLAX_ERR	DOUBLE	Standard error of the stellar parallax (J2015.5)
173	GAIA_PM_RA	DOUBLE	Proper motion in right ascension (mas yr ⁻¹ , J2015.5)
174	GAIA_PM_RA_ERR	DOUBLE	Standard error of the proper motion in R.A. (mas yr ⁻¹ , J2015.5)
175	GAIA_PM_DEC	DOUBLE	Proper motion in declination (mas yr ⁻¹ , J2015.5)
176	GAIA_PM_DEC_ERR	DOUBLE	Standard error of the proper motion in decl. (mas yr ⁻¹ , J2015.5)
177	GAIA_G_MAG	DOUBLE	Mean magnitude in the <i>G</i> band (Vega)
178	GAIA_G_FLUX_SNR	DOUBLE	Mean flux over the standard deviation in the <i>G</i> band (Vega)
179	GAIA_BP_MAG	DOUBLE	Mean magnitude in the <i>BP</i> band (Vega)
180	GAIA_BP_FLUX_SNR	DOUBLE	Mean flux over the standard deviation in the <i>BP</i> band (Vega)
181	GAIA_RP_MAG	DOUBLE	Mean magnitude in the <i>RP</i> band (Vega)
182	GAIA_RP_FLUX_SNR	DOUBLE	Mean flux over the standard deviation in the <i>RP</i> band (Vega)
183	SDSS2GAIA_SEP	DOUBLE	SDSS-Gaia separation in arcseconds

ORCID iDs

Brad W. Lyke  <https://orcid.org/0000-0002-5078-2472>
 Ashley J. Ross  <https://orcid.org/0000-0002-7522-9083>
 Kyle Dawson  <https://orcid.org/0000-0002-0553-3805>
 Paul Martini  <https://orcid.org/0000-0002-4279-4182>
 Hélion du Mas des Bourboux  <https://orcid.org/0000-0001-8955-3573>
 Mara Salvato  <https://orcid.org/0000-0001-7116-9303>
 Julian Bautista  <https://orcid.org/0000-0002-9885-3989>
 Dmitry Bizyaev  <https://orcid.org/0000-0002-3601-133X>
 W. N. Brandt  <https://orcid.org/0000-0002-0167-2453>

Joel R. Brownstein  <https://orcid.org/0000-0002-8725-1069>
 Paul Green  <https://orcid.org/0000-0002-8179-9445>
 Jeffrey A. Newman  <https://orcid.org/0000-0001-8684-2222>
 Nathalie Palanque-Delabrouille  <https://orcid.org/0000-0003-3188-784X>
 Donald P. Schneider  <https://orcid.org/0000-0001-7240-7449>

References

- Abolfathi, B., Aguado, D. S., Aguilar, G., et al. 2018, *ApJS*, 235, 42
 Ahn, C. P., Alexandroff, R., Allende Prieto, C., et al. 2014, *ApJS*, 211, 17
 Aihara, H., Allende Prieto, C., An, D., et al. 2011, *ApJS*, 193, 29

- Alam, S., Albareti, F. D., Allende Prieto, C., et al. 2015, *ApJS*, **219**, 12
 Alam, S., Aubert, M., Avila, S., et al. 2020, arXiv:2007.08991
 Ata, M., Kitaura, F.-S., Chuang, C.-H., et al. 2017, *MNRAS*, **467**, 3993
 Bautista, J. E., Paviot, R., & Vargas Magaña, M. 2020, arXiv:2007.08993
 Becker, R. H., White, R. L., & Helfand, D. J. 1995, *ApJ*, **450**, 559
 Boller, T., Freyberg, M. J., Trümper, J., et al. 2016, *A&A*, **588**, A103
 Bolton, A. S., Schlegel, D. J., Aubourg, É., et al. 2012, *AJ*, **144**, 144
 Bovy, J., Myers, A. D., Hennawi, J. F., et al. 2012, *ApJ*, **749**, 41
 Bruni, G., Piconcelli, E., Misawa, T., et al. 2019, *A&A*, **630**, A111
 Busca, N., & Balland, C. 2018, arXiv:1808.09955
 Calura, F., Tescari, E., D'Odorico, V., et al. 2012, *MNRAS*, **422**, 3019
 Carrasco Kind, M., & Brunner, R. J. 2013, *MNRAS*, **432**, 1483
 Cole, S., Percival, W. J., Peacock, J. A., et al. 2005, *MNRAS*, **362**, 505
 Comparat, J., Merloni, A., Dwelly, T., et al. 2020, *A&A*, **636**, 97
 Cutri, R. M., Skrutskie, M. F., van Dyk, S., et al. 2003, *yCat*, **2246**
 Dawson, K. S., Kneib, J.-P., Percival, W. J., et al. 2016, *AJ*, **151**, 44
 Dawson, K. S., Schlegel, D. J., Ahn, C. P., et al. 2013, *AJ*, **145**, 10
 de Mattia, A., Ruhmann-Kleider, V., Raichoor, A., et al. 2020, arXiv:2007.09008
 du Mas des Bourboux, H., Rich, J., Font-Ribera, A., et al. 2020, arXiv:2007.08995
 Dwelly, T., Salvato, M., Merloni, A., et al. 2017, *MNRAS*, **469**, 1065
 Eisenstein, D. J., Weinberg, D. H., Agol, E., et al. 2011, *AJ*, **142**, 72
 Eisenstein, D. J., Zehavi, I., Hogg, D. W., et al. 2005, *ApJ*, **633**, 560
 Finkbeiner, D. P., Schlafly, E. F., Schlegel, D. J., et al. 2016, *ApJ*, **822**, 66
 Fukugita, M., Ichikawa, T., Gunn, J. E., et al. 1996, *AJ*, **111**, 1748
 Gaia Collaboration, Brown, A. G. A., Vallenari, A., et al. 2018, *A&A*, **616**, A1
 Gil-Marín, H., Bautista, J. E., Paviot, R., et al. 2020, arXiv:2007.08994
 Grier, C. J., Brandt, W. N., Hall, P. B., et al. 2016, *ApJ*, **824**, 130
 Gunn, J. E., Carr, M., Rockosi, C., et al. 1998, *AJ*, **116**, 3040
 Gunn, J. E., Siegmund, W. A., Mannery, E. J., et al. 2006, *AJ*, **131**, 2332
 Guo, Z., & Martini, P. 2019, *ApJ*, **879**, 72
 Hall, K. R., Zakamska, N. L., Addison, G. E., et al. 2019, *MNRAS*, **490**, 2315
 Hall, P. B., Anderson, S. F., Strauss, M. A., et al. 2002, *ApJS*, **141**, 267
 Helfand, D. J., White, R. L., & Becker, R. H. 2015, *ApJ*, **801**, 26
 Hewett, P. C., & Wild, V. 2010, *MNRAS*, **405**, 2302
 Hou, J., Sánchez, A. G., Ross, A. J., et al. 2020, arXiv:2007.08998
 Kaiser, N., Burgett, W., Chambers, K., et al. 2010, *Proc. SPIE*, **7733**, 77330E
 Kollmeier, J. A., Zasowski, G., Rix, H.-W., et al. 2017, arXiv:1711.03234
 Lang, D. 2014, *AJ*, **147**, 108
 Lang, D., Hogg, D. W., & Schlegel, D. J. 2016, *AJ*, **151**, 36
 Law, N. M., Kulkarni, S. R., Dekany, R. G., et al. 2009, *PASP*, **121**, 1395
 Lawrence, A., Warren, S. J., Almaini, O., et al. 2007, *MNRAS*, **379**, 1599
 Lin, S., Tinker, J. L., Klypin, A., et al. 2020, arXiv:2007.08996
 Lupton, R. H., Gunn, J. E., & Szalay, A. S. 1999, *AJ*, **118**, 1406
 MacLeod, C. L., Green, P. J., Anderson, S. F., et al. 2018, *AJ*, **155**, 6
 Martin, D. C., Fanson, J., Schiminovich, D., et al. 2005, *ApJL*, **619**, L1
 McGraw, S. M., Brandt, W. N., Grier, C. J., et al. 2017, *MNRAS*, **469**, 3163
 Morganson, E., Green, P. J., Anderson, S. F., et al. 2015, *ApJ*, **806**, 244
 Myers, A. D., Palanque-Delabrouille, N., Prakash, A., et al. 2015, *ApJS*, **221**, 27
 Neveux, R., Burtin, E., de Mattia, A., et al. 2020, arXiv:2007.08999
 Ofek, E. O., Laher, R., Law, N., et al. 2012, *PASP*, **124**, 62
 Padmanabhan, N., Schlegel, D. J., Finkbeiner, D. P., et al. 2008, *ApJ*, **674**, 1217
 Palanque-Delabrouille, N., Magneville, C., Yèche, C., et al. 2016, *A&A*, **587**, A41
 Pâris, I., Petitjean, P., Aubourg, É., et al. 2012, *A&A*, **548**, A66
 Pâris, I., Petitjean, P., Aubourg, É., et al. 2014, *A&A*, **563**, A54
 Pâris, I., Petitjean, P., Aubourg, É., et al. 2018, *A&A*, **613**, A51
 Pâris, I., Petitjean, P., Ross, N. P., et al. 2017, *A&A*, **597**, A79
 Parks, D., Prochaska, J. X., Dong, S., & Cai, Z. 2018, *MNRAS*, **476**, 1151
 Powell, M. C., Urry, C. M., Cappelluti, N., et al. 2020, *ApJ*, **891**, 41
 Raichoor, A., de Mattia, A., Ross, A. J., et al. 2020, arXiv:2007.09007
 Rau, A., Kulkarni, S. R., Law, N. M., et al. 2009, *PASP*, **121**, 1334
 Richards, G. T., Strauss, M. A., Fan, X., et al. 2006, *AJ*, **131**, 2766
 Rosen, S. R., Webb, N. A., Watson, M. G., et al. 2016, *A&A*, **590**, A1
 Ross, A. J., Bautista, J., Tojeiro, R., et al. 2020, arXiv:2007.09000
 Ross, N. P., Myers, A. D., Sheldon, E. S., et al. 2012, *ApJS*, **199**, 3
 Rossi, G., Choi, P. D., Moon, J., et al. 2020, arXiv:2007.09002
 Ruiz, A., Corral, A., Mountrichas, G., & Georgantopoulos, I. 2018, *A&A*, **618**, A52
 Salvato, M., Buchner, J., Budavári, T., et al. 2018, *MNRAS*, **473**, 4937
 Saxton, R. D., Read, A. M., Esquej, P., et al. 2008, *A&A*, **480**, 611
 Schlafly, E. F., & Finkbeiner, D. P. 2011, *ApJ*, **737**, 103
 Schlafly, E. F., Finkbeiner, D. P., Jurić, M., et al. 2012, *ApJ*, **756**, 158
 Schlegel, D. J., Finkbeiner, D. P., & Davis, M. 1998, *ApJ*, **500**, 525
 Schneider, D. P., Richards, G. T., Fan, X., et al. 2002, *AJ*, **123**, 567
 Schneider, D. P., Richards, G. T., Hall, P. B., et al. 2010, *AJ*, **139**, 2360
 Shen, Y., Brandt, W. N., Dawson, K. S., et al. 2015, *ApJS*, **216**, 4
 Shen, Y., Brandt, W. N., Richards, G. T., et al. 2016, *ApJ*, **831**, 7
 Shen, Y., Richards, G. T., Strauss, M. A., et al. 2011, *ApJS*, **194**, 45
 Sheng, Z., Wang, T., Jiang, N., et al. 2020, *ApJ*, **889**, 46
 Skrutskie, M. F., Cutri, R. M., Stiening, R., et al. 2006, *AJ*, **131**, 1163
 Smee, S. A., Gunn, J. E., Uomoto, A., et al. 2013, *AJ*, **146**, 32
 Smith, A., Burtin, E., Hou, J., et al. 2020, arXiv:2007.09003
 Tamone, A., Raichoor, A., Zhao, C., et al. 2020, arXiv:2007.09009
 Thyagarajan, N., Helfand, D. J., White, R. L., & Becker, R. H. 2011, *ApJ*, **742**, 49
 Timlin, J. D., Brandt, W. N., Ni, Q., et al. 2020, *MNRAS*, **492**, 719
 Vanden Berk, D. E., Richards, G. T., Bauer, A., et al. 2001, *AJ*, **122**, 549
 Wells, D. C., Greisen, E. W., & Harten, R. H. 1981, *A&AS*, **44**, 363
 Weymann, R. J., Morris, S. L., Foltz, C. B., & Hewett, P. C. 1991, *ApJ*, **373**, 23
 Wright, E. L., Eisenhardt, P. R. M., Mainzer, A. K., et al. 2010, *AJ*, **140**, 1868
 Zhao, C., Chuang, C., Bautista, J., et al. 2020, arXiv:2007.08997